

# Dynamics of Jupiter's Atmosphere

**Andrew P. Ingersoll**

*California Institute of Technology*

**Timothy E. Dowling**

*University of Louisville*

**Peter J. Gierasch**

*Cornell University*

**Glenn S. Orton**

*Jet Propulsion Laboratory, California Institute of Technology*

**Peter L. Read**

*Oxford University*

**Agustin Sánchez-Lavega**

*Universidad del País Vasco, Spain*

**Adam P. Showman**

*University of Arizona*

**Amy A. Simon-Miller**

*NASA Goddard Space Flight Center*

**Ashwin R. Vasavada**

*Jet Propulsion Laboratory, California Institute of Technology*

## 6.1 INTRODUCTION

Giant planet atmospheres provided many of the surprises and remarkable discoveries of planetary exploration during the past few decades. Studying Jupiter's atmosphere and comparing it with Earth's gives us critical insight and a broad understanding of how atmospheres work that could not be obtained by studying Earth alone.

Jupiter has half a dozen eastward jet streams in each hemisphere. On average, Earth has only one in each hemisphere. Jupiter has weather patterns ("storms") that last for centuries. Earth has stationary weather patterns fixed to the topography, but the average lifetime of a traveling storm is  $\sim 1$  week. Jupiter has no topography, i.e., no continents or oceans; its atmosphere merges smoothly with the planet's fluid interior. Absorbed sunlight (power per unit area) at Jupiter is only 3.3% that at Earth, yet Jupiter's winds are 3–4 times stronger. The ratio of Jupiter's internal power to absorbed solar power is 0.7. On Earth the ratio is  $2 \times 10^{-4}$ . Jupiter's hydrologic cycle is fundamentally different from Earth's because it has no ocean, but lightning

occurs on both planets. On Earth, electrical charge separation is associated with falling ice and rain. On Jupiter, the separation mechanism is still to be determined.

The winds of Jupiter are only 1/3 as strong as those of Saturn and Neptune, and yet the other giant planets have less sunlight and less internal heat than Jupiter. Earth probably has the weakest winds of any planet, although its absorbed solar power per unit area is largest. All the giant planets are banded. Even Uranus, whose rotation axis is tipped  $98^\circ$  relative to its orbit axis, exhibits banded cloud patterns and east–west (zonal) jets. All have long-lived storms, although Jupiter's Great Red Spot (GRS), which may be hundreds of years old, seems to be the oldest.

### 6.1.1 Data Sets

Early astronomers, using small telescopes with their eyes as detectors, recorded the changing appearance of Jupiter's atmosphere. Their descriptive terms – belts and zones, brown spots and red spots, plumes, barges, festoons, and streamers – are still used. Other terms – describing vorticity,

vertical motion, eddy fluxes, temperature gradients, cloud heights, and wind shear – have been added, bringing the study of Jupiter’s atmospheric dynamics to a level similar to that of Earth during the pioneering days of terrestrial meteorology several decades ago.

Jupiter has what is perhaps the most photogenic atmosphere in the solar system. Most of the visible contrast arises from clouds in the 0.7- to 1.5-bar range (see Chapter 5). The clouds come in different colors, and usually have texture on scales as small as a few tens of kilometers, which is comparable to the  $e$ -folding thickness (scale height) of the atmosphere. At this resolution, cloud tracking over a few hours yields wind estimates with errors of a few  $\text{m s}^{-1}$ . In contrast, the winds around the GRS and many of the zonal jets exceed  $100 \text{ m s}^{-1}$ . Winds are measured relative to System III, a uniform rotation rate with period 9 h 55 m 29.71 s, which is defined by radio emissions that are presumably tied to the magnetic field and thus to the planet’s interior.

Traditional Earth-based telescopic resolution is 3000 km, which is enough to image the major atmospheric features. *Pioneers 10* and *11* improved on Earth-based resolution, but *Voyagers 1* and *2* provided a breakthrough. For cloud tracking, the most important data were the “approach” movies that were recorded during the three months prior to each of the two encounters in March and July of 1979. The spacecraft obtained a view of each feature every  $\sim 10$  hours as the resolution improved from 500 km to 60 km. Occasional views of selected features continued down to a resolution (pixel size) of  $\sim 5$  km. The *Voyager* infrared spectrometer (IRIS) viewed the entire planet at a resolution of several thousand kilometers and obtained spectra of all the major dynamical features. *Galileo* obtained less data than *Voyager*, but the imaging resolution, usually 25 km, and the wavelength coverage were better. In particular, the near-infrared response of the *Galileo* camera allowed imaging in the absorption bands of methane, from which one separates clouds at different altitudes. *Cassini* combined the high data rate of *Voyager* with the broad spectral coverage of *Galileo*, yielding a best resolution of 60 km (the *Cassini* data were still being analyzed at the time of this writing).

Ground-based telescopes and the Hubble Space Telescope (HST) provide a continuous record of Jupiter’s cloud features at several-month intervals. These data document the major events and also the extreme steadiness of the atmosphere. Ground-based telescopes provide the highest spectral resolution. Several trace gases, which provide important diagnostics of vertical motion, were discovered from the ground. Earth-based radio observations probe the deep atmosphere. The HST was essential during the collisions of Comet Shoemaker–Levy 9 with Jupiter in 1994. Besides recording the waves and debris from the collisions, the HST defined the prior dynamical state of the atmosphere.

The *Galileo* probe provided profiles of wind, temperature, composition, clouds, and radiation as functions of pressure down to the 22-bar level, but only at one point on the planet. Except at the *Galileo* probe site, these quantities are uncertain below the 1-bar level. The base of the water cloud is thought to lie at the 6- or 7-bar level,  $\sim 75$  km below the clouds that produce the visible contrast.

## 6.1.2 Scope of the Chapter and Role of Models

This chapter reviews the observations and theory of Jupiter’s atmospheric dynamics. Sections 6.2 and 6.3 cover the banded structures and discrete features, respectively. Section 6.4 covers vertical structure and temperatures. Section 6.5 discusses lightning and models of moist convection. Section 6.6 reviews numerical models of the bands and zonal jets, and Section 6.7 reviews numerical models of the discrete features. Finally, Section 6.8 provides a discussion of outstanding questions and how they might be answered. The chapter is aimed at a general planetary science audience, although some familiarity with atmospheric dynamics is helpful for the modeling sections.

As in the terrestrial atmospheric sciences, validated numerical models are the key to understanding. Models of Jupiter’s atmosphere tend to be less complex than models of Earth’s atmosphere. They nevertheless contain much of the nonlinear physics associated with large-scale stratified flows in rotating systems. Ideally, the complexity of the models matches that of the observations, so that hypotheses can be tested cleanly. Some pure fluid dynamics models, e.g., of two-dimensional flows without viscosity, find their best applications on Jupiter and the other giant planets. Examples include the Kida vortex model, the models of inverse cascades and beta-turbulence, and the statistical mechanical models of two-dimensional coherent structures. These models are discussed in Sections 6.6 and 6.7.

Peek (1958) is the definitive book for early observations of Jupiter’s atmosphere. Gehrels (1976) is a collection of chapters by various authors following the *Pioneer* encounters. Rogers (1995) is the modern equivalent of Peek. There are many review articles (Ingersoll 1976b, Stone 1976, Williams 1985, Beebe *et al.* 1989, Ingersoll 1990, Marcus 1993, Gierasch and Conrath 1993, Dowling 1995a, Ingersoll *et al.* 1995). As an ensemble, the articles record the variance of expert opinion. As a time series, they record the progress that has been made and bring clarity to the remaining unanswered questions.

For a point on the surface of an oblate planet, there are two definitions of latitude. Planetographic (PG) latitude is the elevation angle (relative to the equatorial plane) of the vector along the local vertical, and planetocentric (PC) latitude is the elevation angle (relative to the equatorial plane) of the vector from the planet’s center. PG latitude is greater than PC latitude except at the equator and poles where they are equal. For Jupiter the maximum difference ( $4.16^\circ$ ) is at  $46.6^\circ$  PG latitude. Unless otherwise specified, we use PG latitudes in this chapter.

## 6.2 BANDED STRUCTURE

### 6.2.1 Belts and Zones

Jupiter’s visible atmosphere is dominated by banded structures (Figure 6.1). Traditionally, the white bands are called zones and the dark bands are called belts. The zonal jets (eastward and westward currents in the atmosphere) are strongest on the boundaries between the belts and zones (Figure 6.2). The zones are anticyclonic, which means they have an eastward jet on the poleward side and a westward jet on the equatorward side (in the reference frame of the planet,

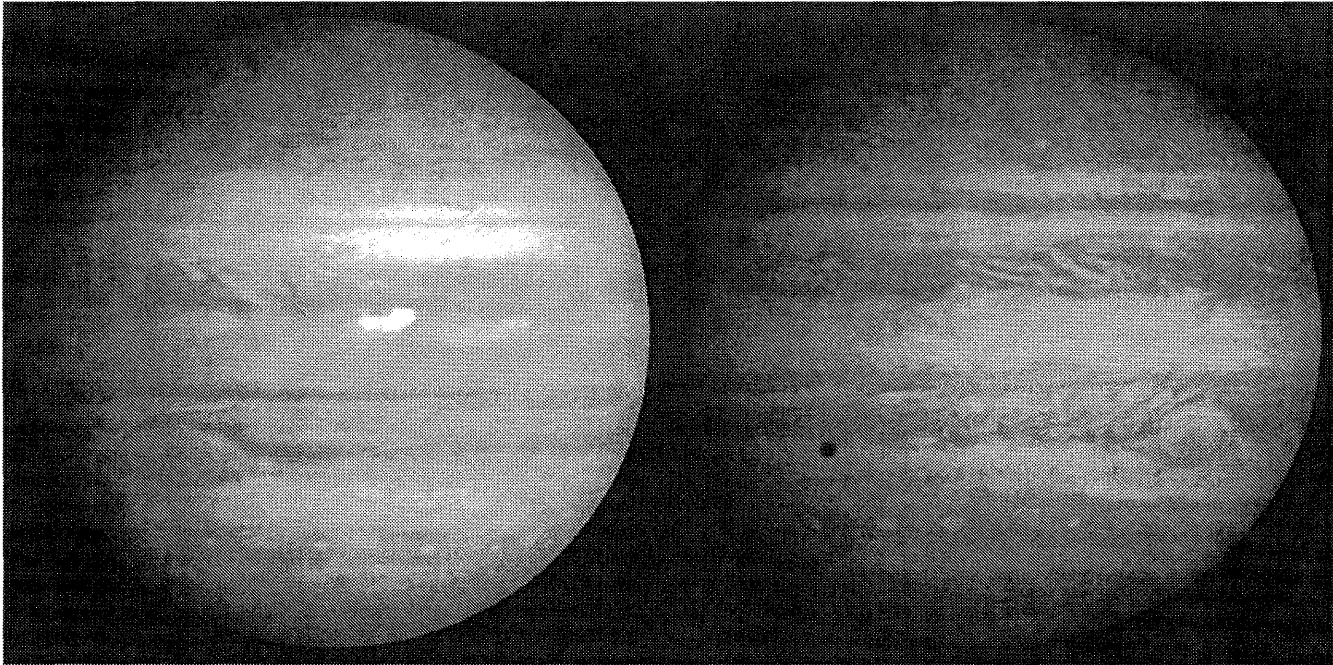


**Figure 6.1.** Whole disk views of Jupiter. The left image is from *Voyager 2* in June 1979. The right image is from *Cassini* in November 2000. At the time of going to press a colour version of this figure was available for download from <http://www.cambridge.org/9780521035453>.

an anticyclone rotates clockwise in the northern hemisphere and counterclockwise in the southern hemisphere). The belts are cyclonic, which means they rotate the opposite way. In an inertial frame, the rotation period varies with latitude in a range  $\pm 5$  min on either side of the System III period. The major belts and some inertial rotation periods are labeled in Figure 6.3 (Peek 1958, Stone 1976). Individual features like the GRS tend to have the same sign of vorticity (sense of rotation) as the band in which they sit.

Jupiter is not bright orange or red in color, but more of a muted brown (Peek 1958, Simon-Miller *et al.* 2001a). The colors of the belts and zones vary with time. The origin of the colors and how they respond to the winds are uncertain. The major cloud constituents – ammonia,  $\text{H}_2\text{S}$ , and water – are colorless, but elemental sulfur, phosphorus, and organic compounds could combine in trace amounts to form the muted colors.

The zones appear more uniform than the belts, particularly in the northern hemisphere. In the zones the small-scale texture has low contrast. The large-scale features in the zones are generally steadier in time than those in the belts. The clouds in the zones generally extend to higher altitudes than those in the belts; the corresponding pressure difference is a few hundred mbar. The gaseous ammonia abundance is higher in the zones, and the upper tropospheric temperatures are lower (Conrath and Gierasch 1986, Gierasch *et al.* 1986, Simon-Miller *et al.* 2001b). The darker belts have deeper clouds overall and more variation in cloud height. There are holes in the visible cloud deck (5- $\mu\text{m}$  hot spots, Figure 6.4) that allow radiation to escape from the warmer layers below (Terrile and Westphal 1977, Ortiz *et al.* 1998); this radiation is most intense in a narrow wavelength region around 5  $\mu\text{m}$  where there are no gaseous absorption lines to impede it. The belts are the sites of initially small convective events that sometimes grow to great heights and encir-

cle the entire planet (Beebe *et al.* 1989, Simon-Miller *et al.* 2001b). Amateur and professional observers have recorded many such disturbances (e.g., Sánchez-Lavega *et al.* 1991, Sánchez-Lavega and Gomez 1996, Rogers 1995). Although the belt/zone boundaries align closely with the zonal jets, they do change in latitudinal extent and can recede or extend beyond the cores of the jets (Beebe *et al.* 1989, Rogers 1995, Simon *et al.* 1998).

Imbedded in the zones are the major anticyclonic ovals like the GRS at  $22.5^\circ\text{S}$ , the White Ovals at  $33^\circ\text{S}$ , and smaller ovals at  $41^\circ\text{S}$ ,  $34^\circ\text{N}$ ,  $40^\circ\text{N}$ , and  $45^\circ\text{N}$  PG latitudes. These ovals usually extend into the neighboring belt on the equatorward side, and sometimes block it off. Then the belt becomes a series of closed cyclonic cells, each one spanning the region between two anticyclonic ovals. Activity is greatest on the eastern end of each cyclonic cell, giving it the appearance of a turbulent wake extending off to the west of the anticyclonic oval. The best example is the South Equatorial Belt (SEB), whose active part extends westward, just north of the GRS. Both the SEB and the North Equatorial Belt (NEB) are sites of intense convective activity – lightning storms with high, thick clouds that double in area in less than half a day (Gierasch *et al.* 2000).

Jupiter's Equatorial Zone (EZ) lies between the eastward jets at PG latitudes  $\pm 7^\circ$ . The vorticity is anticyclonic (clockwise north of the equator and counterclockwise south of the equator), but the EZ is different from other zones. Methane band images that sound the upper troposphere reveal an elevated haze that is thicker than that at neighboring latitudes. Visible band images reveal a bland cloud deck whose northern boundary is punctuated by a dozen 5- $\mu\text{m}$  hot spots and plumes (Ortiz *et al.* 1998). The latter are high, thick clouds that trail off 10 000 km to the southwest. The plume heads are located just west of the hot spots and sometimes exhibit convective activity (Hunt *et al.* 1981).

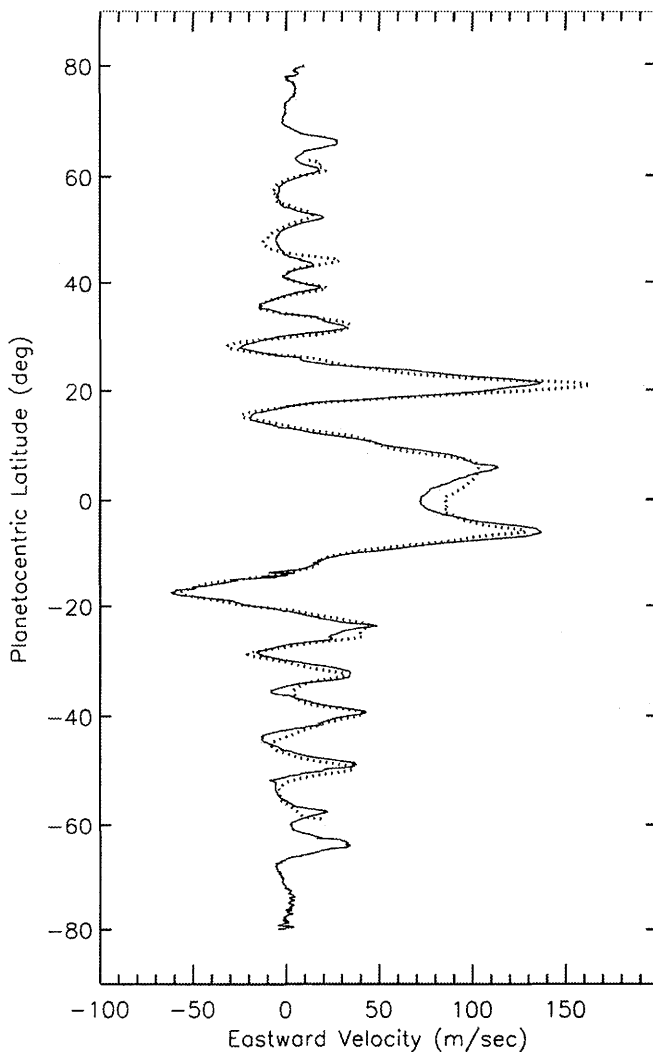


**Figure 6.2.** Zonal winds vs. latitude in 1979 and 2000. The dashed line is from *Voyager* (Limaye 1986), and the solid line is from *Cassini* (Porco *et al.* 2003).

The *Galileo* probe entered on the southern edge of a hot spot at PG latitude  $6.5^{\circ}\text{N}$  (Orton *et al.* 1998). Neither plumes nor hot spots look like vortices; nevertheless non-zonal motions have been associated with them (Vasavada *et al.* 1998). Between 10–13 hot spot/plume pairs have been present since the *Voyager* era; however *Pioneer* images and historical records indicate that there may have been fewer in the past. The train of features translates to the east with a velocity of  $\sim 100\text{ m s}^{-1}$ . When this translation is removed from time-series images of Jupiter's equator, the growth, interactions, and decay of individual features over months to years become apparent (Ortiz *et al.* 1998). *Cassini* movies, *Galileo* probe results, and numerical simulations suggest that the features are probably a nonlinear wave traveling westward on a fast ( $\sim 160\text{ m s}^{-1}$ ) eastward jet (Showman and Dowling 2000).

The banded appearance at low latitudes gradually gives way at mid latitudes to a mottled appearance at high latitudes, which are dominated by closely spaced anticyclonic ovals and cyclonic features (Figure 6.5). Despite this mottled appearance, movies show that organized zonal mo-

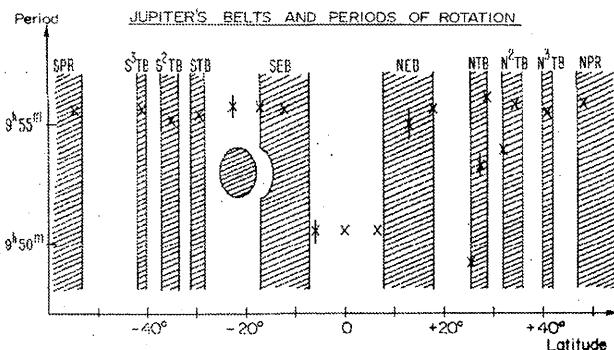


**Figure 6.3.** Jupiter's belts and zones and periods of rotation. The figure is from Stone (1976), who used data summarized by Peek (1958). Those data were derived from decades of Earth-based telescopic observations. The belts are NEB = North Equatorial Belt, NTB = North Temperate Belt,  $\text{N}^2\text{TB}$  = North North Temperate Belt, etc., and similarly in the south. The zones are EZ = Equatorial Zone, NTrZ = North Tropical Zone, NTZ = North Temperate Zone,  $\text{N}^2\text{TZ}$  = North North Temperate Zone, etc., and similarly in the south. Periods are measured by tracking features larger than  $\sim 3000\text{ km}$  over time intervals of days or weeks. Short periods represent flow to the east relative to System III, which is the  $9\text{ h } 55\text{ m } 29.71\text{ s}$  period defined from radio frequency observations.

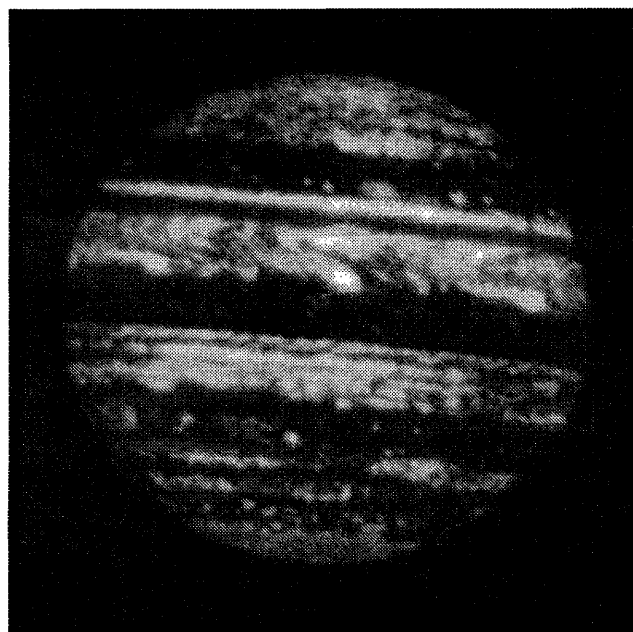


**Figure 6.4.** Whole disk image at a wavelength of  $5\text{ }\mu\text{m}$  (Ortiz *et al.* 1998). The brightest areas, termed  $5\text{-}\mu\text{m}$  hot spots, are holes in the visible cloud deck that reveal the warmer, deeper layers below. Maximum brightness temperatures sometimes exceed  $273\text{ K}$ . The *Galileo* probe entered on the south edge of a hot spot at  $6.5^{\circ}\text{N}$  latitude.

tions extend to  $\pm 80^{\circ}$  at least (Garcia-Melendo and Sánchez-Lavega 2001, Porco *et al.* 2003). Methane-band images display prominent polar caps of elevated and thicker haze, possibly maintained by auroral processes, with wave-like boundaries (Rages *et al.* 1999, Sánchez-Lavega *et al.* 1998a, Chapter 5). Recent observations at ultraviolet wavelengths, which

are sensitive to stratospheric aerosols, reveal vortices and other features clearly distinct from those of the visible cloud deck and possibly associated with the auroral footprint (Vincent *et al.* 2000, Porco *et al.* 2003).

### 6.2.2 Changes in Appearance

Although Jupiter's banded appearance is quite stable, changes are visible in the *Voyager* and *Cassini* images acquired in 1979 and 2000, respectively (Figure 6.1). The equatorial plumes were less well defined with respect to their surroundings in 2000 than they were in 1979, although they were present in roughly the same numbers. There was a reversal in the north-to-south color gradient across the EZ as well (Simon-Miller *et al.* 2001b).

The NEB was more active around the time of the *Cassini* flyby. Dark material extended further to the north than in the *Voyager* era. Many active sites were visible, and possible brown barges (elongated cyclonic dark ovals not visible in Figure 6.1) were reported for the first time since the *Voyager* era (neither HST nor *Galileo* saw brown barges in the 1990 to mid-2000 time period). The North Temperate Belt (NTB, from 23°N to 31°N), showed more contrast with respect to the surrounding zones than in the *Voyager* era. None of these changes is particularly unusual. The belts and zones often change color or width. Good historical accounts of similar events are found in Peek (1958) and Rogers (1995). Detailed studies of recent disturbances in the SEB and NTB can be found in Sánchez-Lavega and Gomez (1996) and Sánchez-Lavega *et al.* (1991), respectively.

The GRS decreased in longitudinal extent and became much rounder in appearance during the 21 years between the *Voyager* and *Cassini* epochs. The three largest white ovals (not visible in the *Cassini* image) also decreased in size and eventually merged into a single vortex. The small ovals at 41°S have not changed in appearance or number. Despite the slight differences in the ovals and belt/zone appearance, the overall appearance of the planet and its major features in both frames of Figure 6.1 is remarkably unchanged.

### 6.2.3 Changes in Zonal Velocity

The velocities of Jupiter's zonal jets have been inferred from the translation of cloud features for hundreds of years (Peek 1958, Smith and Hunt 1976). Uncertainties arise from different instruments and wavelengths, inaccurate image navigation, changes in the morphology of tracked cloud features, confusion of measurements by non-zonal circulations, and imperfect coupling of tracked features to the underlying zonal flow (e.g., Beebe *et al.* 1996). Nevertheless *Voyager*, *Galileo*, HST, and *Cassini* images have produced a 21-yr record of high-quality velocity measurements capable of revealing any decadal-scale variations greater than about 10 m s<sup>-1</sup> (Figure 6.2). The number and magnitude of Jupiter's jets have remained virtually unchanged, in spite of the presence of turbulence, convection, uncertainty in altitude, and major changes in the brightness and width of the bands. The measured winds probably refer to levels in the 0.7- to 1.0-bar range (Banfield *et al.* 1998).

Some minor variations in jet shape and speed have been reproduced by several analyses, however, including the results shown in Figure 6.2 (Limaye 1986, Vasavada *et al.* 1998,

Simon 1998, Garcia-Melendo *et al.* 2001, Porco *et al.* 2003). Between 1979 and 1995 the eastward jet at 23°N slowed from 180 m s<sup>-1</sup> to 140 m s<sup>-1</sup> and then remained constant. The westward jet at 30°N and the jets between 40°N and 55°N also show significant (10–20 m s<sup>-1</sup>) changes and small shifts in latitude.

### 6.2.4 Two Hypotheses about the Banded Structure

Jupiter's large-scale winds are in approximate geostrophic balance; therefore anticyclones are high-pressure centers and cyclones are low-pressure centers. Warm-core features (warmer than their surroundings at the same pressure level) become more anticyclonic with altitude because pressure decreases with altitude more slowly when the air is warm than when it is cold. By the same token, cold-core features become more cyclonic with altitude. Thus in the Earth's atmosphere, a warm-core feature like a hurricane changes from strongly cyclonic at low altitude to weakly anticyclonic at high altitude. And in the Earth's ocean, warm-core features may be weakly cyclonic or anticyclonic at depth, but they become strongly anticyclonic at the ocean surface. These are examples of a quantitative relation between wind shear and horizontal temperature gradient called the thermal wind equation (e.g., Pedlosky 1987).

For Jupiter, the traditional view (Hess and Panofsky 1951, Ingersoll and Cuzzi 1969) is that the winds are weak in the deep atmosphere as in the deep oceans; in other words, the winds that we see are shallow. This implies that the zones and anticyclonic ovals are warm-core features – the air between the deep “level of no motion” and the surface on which the winds are measured is warmer than the surroundings. Since warm air tends to rise and cold air tends to sink, it is natural to assume that the air in the zones is slowly rising and the air in the belts is slowly sinking. And since clouds tend to form on updrafts, this view seems to be consistent with the observation that the visible cloud deck is higher in the zones (and in the anticyclonic ovals) and lower in the belts. This view also seems to be consistent with the observation that the 5- $\mu$ m hot spots, which are holes in the visible cloud deck, are concentrated in the belts (Terre and Westphal 1977).

An alternate view (Busse 1976) is that the winds are just as strong in the deep atmosphere as they are in the visible cloud deck. If the fluid is barotropic, meaning that temperature is constant at constant pressure, the zonal jets would be the surface manifestation of differentially rotating cylinders concentric with the planet's rotation axis (Poincaré 1910). The fluid would then move in columns, according to the so-called Taylor–Proudman theorem (e.g., Pedlosky 1987). On the other hand, if the fluid is baroclinic, meaning that temperature varies at constant pressure, the winds would not obey the Taylor–Proudman theorem and the fluid would not move in columns. Distinguishing between these two extremes, shallow *vs.* deep, requires knowledge of winds and temperatures in the deep atmosphere.

### 6.2.5 Evidence of Upwelling and Downwelling

Large-scale vertical velocities are estimated to be  $\sim 10^{-3}$  m s<sup>-1</sup>, which is too small to be measured directly. Departures

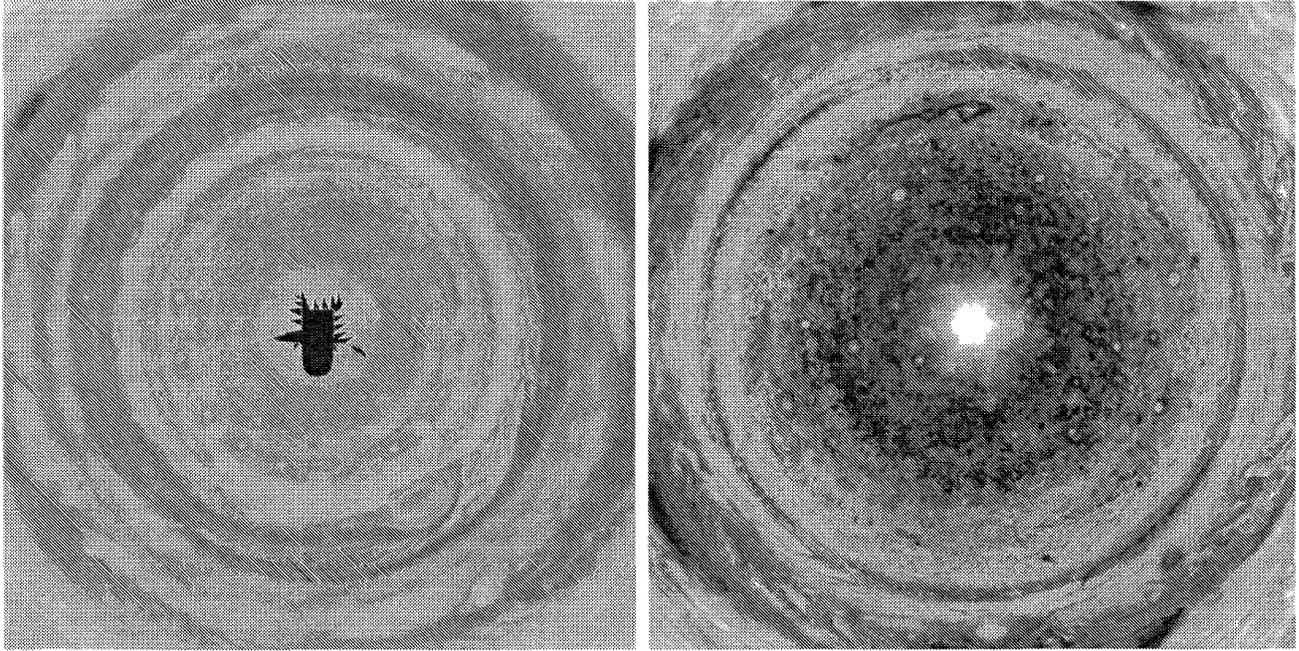


**Figure 6.5.** Polar views of Jupiter. Images from different longitudes were map projected to show, from a viewpoint directly over the pole all the features in sunlight at the same time. Latitude varies linearly with radial distance in the image, from  $0^\circ$  in the corners to  $90^\circ$  in the center. (Left) South pole in 1979 from *Voyager*. (Right) North pole in 2000 from *Cassini*.

from chemical and thermal equilibrium provide indirect evidence of vertical velocity when the equilibrium state is a function of altitude. We consider four examples. The first involves the fraction of  $\text{H}_2$  molecules in the two possible spin states, ortho and para. The equilibrium para fraction decreases with depth due to the increase in temperature, so a para fraction below the equilibrium value is a sign of upward motion. Second, a stably stratified atmosphere is one in which the potential temperature (or equivalently, the entropy) increases with height; therefore rising air tends to have low potential temperature and sinking air tends to have high potential temperature. It follows that when there are no other heat sources, low and high temperatures mean upwelling and downwelling, respectively. Third, ammonia condenses and precipitates in the upper troposphere, so high ammonia abundance is generally a sign of upwelling. Fourth, clouds form on updrafts, so increased cloud optical thickness is generally a sign of upwelling.

The *Voyager* IRIS spectra allow simultaneous determination of the ortho–para ratio, the temperature, the ammonia concentration, and cloud optical depths at two different wavelengths (5 and 45  $\mu\text{m}$ ), all with spatial resolution of a few thousand km over most of the planet. The temperature and para fraction refer to pressure levels of a few hundred mbar; the 45- $\mu\text{m}$  cloud optical depth and the ammonia concentration refer to levels between 1 bar and space; and the 5- $\mu\text{m}$  optical depth refers to levels between a few bars and space (Conrath and Gierasch 1986). An orderly pattern related to the zonal mean jets emerges from these measurements (Gierasch *et al.* 1986). Upper tropospheric temperatures are higher over the belts than over the zones, implying that the zones lose their anticyclonic vorticity and the belts lose their cyclonic vorticity as altitude increases,

i.e., the winds get weaker with altitude. Figure 6.6 compares the thermal wind shear  $\partial\bar{u}/\partial z$ , computed from the measured temperature gradient  $\partial\bar{T}/\partial y$ , with the mean zonal wind  $\bar{u}$  measured by cloud tracking, where  $y$  and  $z$  are the northward and upward coordinates, respectively. This decay of the zonal winds with altitude takes place over two or three scale heights. Cloud optical depths and ammonia abundance are displayed in Figure 6.7, and a ground-based 5- $\mu\text{m}$  image is shown in Figure 6.4 (Orton *et al.* 1996, 1998). Regions of low 5- $\mu\text{m}$  optical depth appear bright because they allow thermal radiation from below to escape. The belts are regions of low optical depth and low ammonia abundance. The inference is that the air in the belts is sinking, at least within the upper troposphere (from 0.1 to 0.5 bars). Under this interpretation, the mean meridional motions (longitudinally averaged motions in the vertical and north–south directions) agree with the traditional view of zones as sites of upwelling and belts as sites of downwelling.

The temperatures of the upper troposphere (warm belts, cold zones) are opposite to those postulated for the lower troposphere according to the traditional view based on a level of no motion below the visible cloud deck. Yet in both cases one infers rising motion in the zones and sinking motion in the belts. The difference is that in the upper troposphere there are no obvious heat sources that would make the belts warmer – one has to invoke downwelling. In the lower troposphere one can invoke latent heat to keep the zones warmer (Ingersoll and Cuzzi 1969, Barcilon and Gierasch 1970).

The inferred circulation in the upper troposphere has hot air *sinking* and cold air *rising*. This is a thermally indirect circulation, which stores potential energy and must be mechanically driven. Gierasch *et al.* (1986) and Conrath

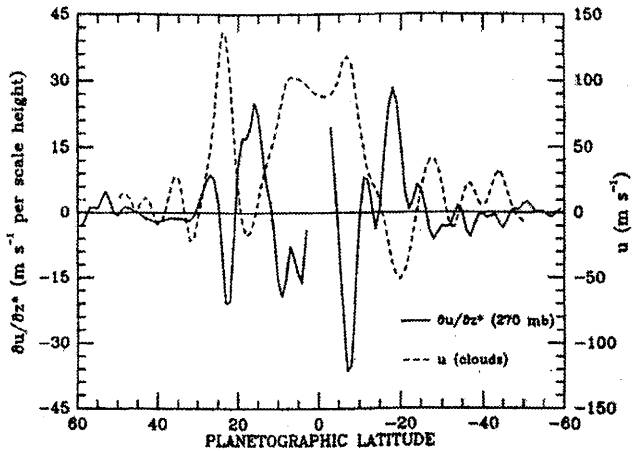


**Figure 6.6.** Upper tropospheric ( $\sim 270$  mbar) thermal wind shears compared with cloud-tracked wind velocities. The figure is from Gierasch *et al.* (1986), who computed the thermal wind shears from *Voyager* IRIS data. The cloud-tracked winds are from Limaye (1986) and refer to the  $\sim 0.7$  bar level.

*et al.* (1990) argue that the mean zonal flow at cloud-top level provides the energy. That flow is subject to dissipation, which they parameterize as Rayleigh drag and Newtonian radiative damping. The dissipation causes the zonal winds to decay with altitude. The upwelling and downwelling above the clouds are part of a mean meridional overturning that balances the dissipative effects with Coriolis acceleration and vertical advection of potential temperature. Pirraglia (1989) and Orsolini and Leovy (1993a, 1993b) show that shear instability produces large-scale eddies that give the required decay of jets within the upper troposphere. The instabilities thus may be the physical process underlying the drag coefficient parameterization in the interpretation by Gierasch *et al.* (1986).

West *et al.* (1992) and Moreno and Sedano (1997) have calculated the residual mean meridional circulation (in the altitude–latitude plane) taking into account the belt-zone temperature differences as well as the absorbing aerosols that are found especially over the polar regions. Such aerosols increase the solar heating rates, and result in a hemisphere-wide circulation from 1 to 100 mbar. The belt-zone downwellings and upwellings were found to persist only up to the vicinity of the tropopause at  $\sim 100$  mbar.

The hydrogen para fraction shows a large-scale gradient from a minimum near the equator to higher values near the poles, which is consistent with upwelling near the equator and sinking near the poles, but it does not show a systematic correlation with belts and zones the way the clouds and ammonia do (Gierasch *et al.* 1986). However these ortho-para data from the IRIS spectra refer to a higher level in the upper troposphere (a few hundred mbar) than do the cloud optical depths and the ammonia concentration, and thus may be diagnostic of a different dynamical regime.

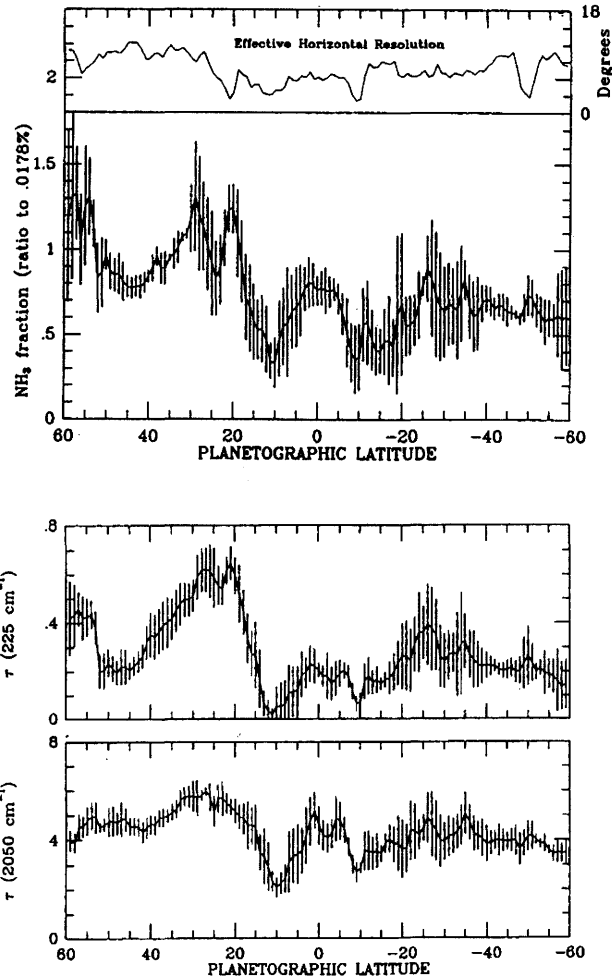


**Figure 6.7.** Estimates of zonal mean ammonia concentration, 5- $\mu\text{m}$  cloud optical depth ( $2050\text{ cm}^{-1}$ ), and 45- $\mu\text{m}$  cloud optical depth ( $225\text{ cm}^{-1}$ ) from *Voyager* IRIS spectra. Absolute values of these retrieved quantities are model dependent, but the relative values from latitude to latitude are reliable. Ammonia and 45- $\mu\text{m}$  cloud refer to levels between about 1 bar and space, and 5- $\mu\text{m}$  cloud refers to levels between a few bars and space. All three quantities correlate well with continuum brightness in the visible (Gierasch *et al.* 1986).

## 6.3 DISCRETE FEATURES

### 6.3.1 Great Red Spot

The GRS is probably the largest and oldest vortex in the atmospheres of the planets. Its oval shape appears in drawings from 1831, but it was tentatively first observed by J. P. Cassini and others from 1665 to 1713 (Rogers 1995). Measurements in 1880 showed that it had an east–west length of 39 000 km and a north–south width of 12 500 km. Its east–west length has decreased since then to its present 17 000 km (Beebe and Youngblood 1979, Rogers 1995, Simon-Miller *et al.* 2002). The GRS is an anticyclonic vortex (high pressure center) extending from  $17^\circ\text{S}$  to  $27.5^\circ\text{S}$  PG latitude. In 1979 it had a maximum velocity of  $120\text{ m s}^{-1}$  along a peripheral collar and maximum relative vorticity  $\sim 6 \times 10^{-5}\text{ s}^{-1}$ , which is about 1/3 the local planetary vorticity (vorticity due to the planet’s rotation). As shown in Figure 6.8, its central

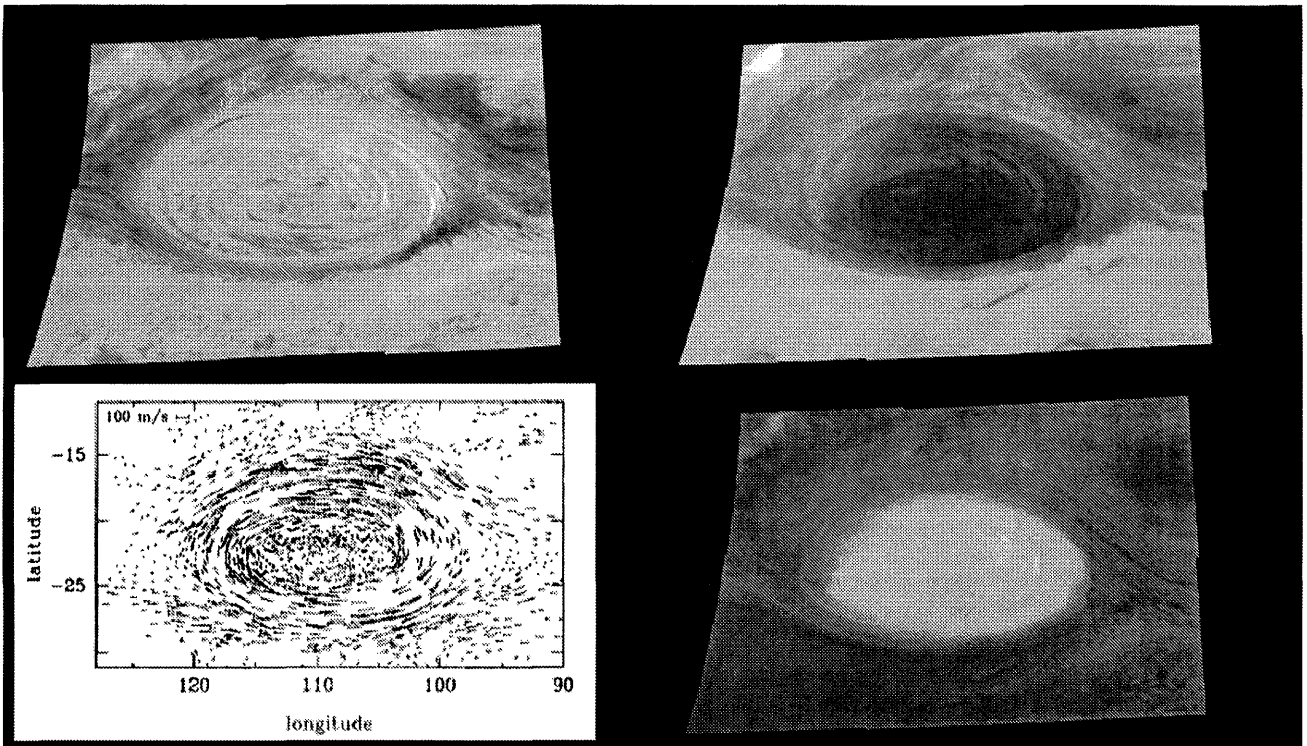


**Figure 6.8.** GRS in three filters with measured velocities. The images are from *Galileo* and the velocities are from *Voyager* (Dowling and Ingersoll 1988). The flow is a counterclockwise high-speed jet with a quiet region inside. The upper left panel is a continuum filter image at 756 nm. The upper right panel is a violet image at 410 nm. The lower right panel is a methane band image at 889 nm. High clouds appear bright at 889 nm. Two regions with high clouds are visible in the image – the interior of the GRS, which is relatively quiet, and the small region in the upper left corner, which is short-lived and active. Lightning often appears in these active regions, which are probably sites of moist convection.

parts are quiescent (Mitchell *et al.* 1981, Dowling and Ingersoll 1989, Sada *et al.* 1996, Vasavada *et al.* 1998). Recent measurements from *Galileo* images indicate an increase in maximum tangential velocities to  $190 \text{ m s}^{-1}$  (Simon-Miller *et al.* 2002).

*Voyager*, *Galileo*, and recent *Cassini* temperature measurements show that the GRS has a cold core at upper tropospheric levels (Flasar *et al.* 1981, Orton *et al.* 1996, Simon-Miller *et al.* 2002) with a peripheral ring of high  $5\text{-}\mu\text{m}$  emission (Terrile and Beebe 1979). Figure 6.9 shows a temperature map obtained by the *Galileo* PPR instrument. The cold temperatures over the GRS indicate that the anticyclonic vorticity decays with height, reaching zero at  $P \sim 50$  mbar (Flasar *et al.* 1981). The para fraction shows a minimum within the GRS, which is consistent with an upwelling, zone-like, anticyclonic behavior (Sada *et al.* 1996, Simon-Miller *et al.* 2002).

Photometry from the UV to the near-IR indicates that the GRS has one main cloud deck at 0.7 bar that is overlain by a dense tropospheric blue-absorbing haze at about 200 mbar and an uppermost thin stratospheric haze extending to  $P \sim 10$  mbar (Banfield *et al.* 1998). There are significant internal variations from point to point (Simon-Miller *et al.* 2002). The GRS is dark at violet and blue wavelengths, giving it a brick-red color. The chemical agent responsible for this color is unknown. The combined data show that the GRS cloud deck slopes upward from south to north, as

do streamlines in the circulating current around the GRS (Simon-Miller *et al.* 2002).

During the period 1880–2002, the GRS moved westward relative to System III with an average speed of  $3 \text{ m s}^{-1}$ . The speed varies slowly on a long (multi-year) timescale. Superposed on this motion, the GRS oscillates in longitude with a period of 90 days and peak-to-peak amplitude of  $\sim 1^\circ$  (Solberg 1969, Trigo-Rodriguez *et al.* 2000). This motion is perturbed when the GRS interacts with features drifting relative to it in nearby latitudes. The GRS engulfs the smaller anticyclones of size  $\sim 2000$  km and position PG latitude  $\sim 20^\circ\text{S}$  that approach from the east with a speed of  $50 \text{ m s}^{-1}$  (Smith *et al.* 1979a, Mac Low and Ingersoll 1986). On other occasions, before they reach the GRS these small vortices are deflected southward into the eastward current at PG latitude  $27^\circ\text{S}$  by a dark curved feature (Peek 1958, Smith *et al.* 1979b), the so-called South Tropical Zone Disturbance (STrZD), which forms sporadically. Several encounters between the GRS and the STrZD have been documented in detail (Smith *et al.* 1979b, Sánchez-Lavega and Rodrigo 1985, Rogers 1995). In 1997 the GRS interacted with a 14-year old, 8000 km anticyclone at  $21.5^\circ\text{S}$  (the White Tropical Oval), absorbing part of its material and expelling the rest (Sánchez-Lavega *et al.* 1998b). On the equatorward side the GRS sometimes generates a stable plume-like feature at  $6^\circ\text{S}$  that compresses the white material in the SEB (Sánchez-Lavega and Rodrigo 1985). These interactions produce transient accelerations and decelerations in the GRS motion.

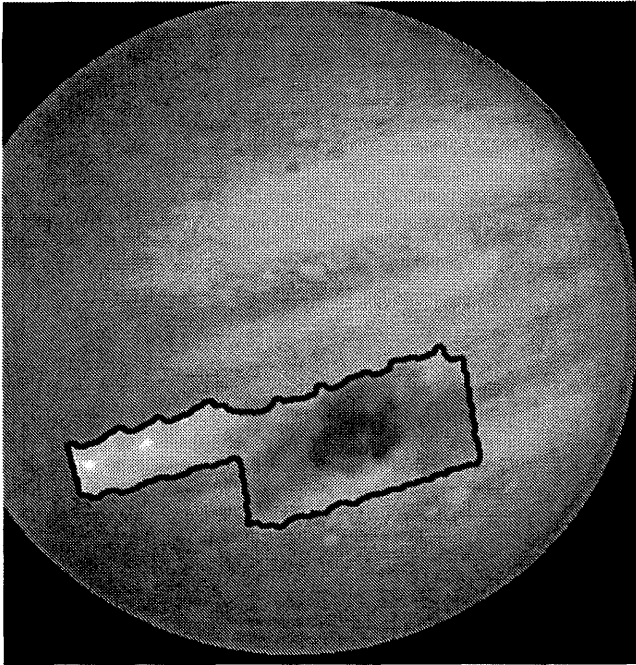


**Figure 6.9.** *Galileo* PPR images of the GRS. The instrument records thermal emission from the gas in the upper troposphere, where the GRS is some 10 K colder than its surroundings. Since there are no radiative processes to account for these cooler temperatures, they are most likely due to upwelling of air with lower potential temperature.

### 6.3.2 White Ovals and Other Anticyclones

The GRS is the largest anticyclonic oval, but it is not unique. Most of the others are white, but some are red. White ovals are most conspicuous near PG latitudes  $33^{\circ}\text{S}$  and  $41^{\circ}\text{S}$  but also occur near  $17^{\circ}\text{N}$ ,  $34^{\circ}\text{N}$  and  $40^{\circ}\text{N}$ . The major diameter ranges from  $\sim 1000$  km to over 5000 km. The ones at high latitudes are smaller and rounder than those at low latitudes (Mac Low and Ingersoll 1986, Morales-Juberías *et al.* 2002a). The ratio of meridional to zonal extent approaches unity for the smallest ovals.

The three large white ovals at  $33^{\circ}\text{S}$  (termed BC, DE, and FA) formed when an anticyclonic, planet-encircling zone, the STZ, broke into three parts in 1939–40 (Peek 1958, Beebe *et al.* 1989, Rogers 1995). The ovals were similar in appearance and size (minor and major axes about 5000 and 10 000 km) but exhibited varied longitudinal drift rates (possibly correlated with latitude), spacing, and interactions with neighboring cyclonic features and the GRS. In the late 1990s, the eastward drift rate of oval BC slowed, causing the other ovals and intervening cyclonic features to pile up (compress) on the westward side of BC (Simon *et al.* 1998). In early 1998, ground-based telescopes documented the merger of ovals BC and DE into a larger oval and possibly a small, cyclonic vortex (Sánchez-Lavega *et al.* 1999). Figure 6.10 shows BC and DE just before their merger, with a vastly reduced cyclonic region squeezed in between them. Two years later the new oval merged with FA (Sánchez-Lavega *et al.* 2001) to form a single oval named BA.

Ovals form in several ways. Small ovals ( $<1000$  km) may form in updrafts (e.g., thunderstorm clusters) whose spreading motion produces anticyclonic vorticity. Ovals may

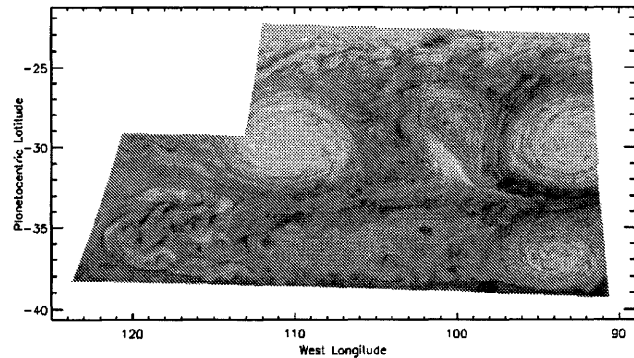


**Figure 6.10.** *Galileo* image of white ovals DE and BC shortly before their merger in 1998 (Vasavada *et al.* 1998). The ovals DE (left) and BC (right) are at  $30^{\circ}\text{S}$  planetocentric latitude. They are anticyclones (counterclockwise in the southern hemisphere), and there is a cyclonic region between them. The eastward current at  $32^{\circ}\text{S}$  flows south of DE and creates the white cloud on the west side of the cyclonic region. It then flows north, clockwise around the cyclonic region, and finally south of BC and out of the figure to the east. The white oval to the south did not participate in the merger.

also form when an anticyclonic zone breaks up, as the STZ did in 1939–40. Ovals disappear by merging and by getting stretched out in the large-scale shear flow. Observations and dynamical simulations suggest that within each mid-latitude zone ovals ingest or merge with others, suggesting that they would grow in size until one or a few dominate (Mac Low and Ingersoll 1986, Dowling and Ingersoll 1989). However, historical observations reveal that the semi-major axes of the largest white ovals and the GRS decrease over time (Simon-Miller *et al.* 2002).

The anticyclonic rotation of the largest white ovals is well defined by their interior cloud texture. Tangential velocity increases approximately linearly with radial distance out to the visual boundary (Mitchell *et al.* 1981, Vasavada *et al.* 1998). Like the GRS, the white ovals are cold at upper troposphere levels, even after mergers (Sánchez-Lavega *et al.* 1999, 2001). Their anticyclonic vorticity, the presence of colder upper-level temperatures, the observed increased altitude of overlying hazes, their bright, white coloration and dark halos all suggest moderate upwelling within white ovals (Conrath *et al.* 1981, Banfield *et al.* 1998). The GRS is distinguished from white ovals by its annular velocity structure (surrounding an interior with little organized motion) and its coloration, which may indicate its greater ability to dredge and/or confine trace species. Little red spots have occasionally been seen in the NTrZ, which is the northern counterpart of the STZ where the GRS resides (Beebe and Hockey 1986). These small anticyclones have the same characteristic UV absorber that is present in the GRS but is not present in the belts.

### 6.3.3 Cyclonic Features

The cyclonic regions tend to be more spread out in the zonal direction than the anticyclonic ovals. They have a more chaotic, filamentary texture and tend to evolve more rapidly, though some survive for a few years. The cyclonic

regions contain a variety of organized morphologies that can be grouped in the following main categories (Smith *et al.* 1979a, 1979b, Mitchell *et al.* 1979, Morales-Juberias *et al.* 2002b): (1) filamentary turbulence related to the highest-speed jets in the SEB (west of the GRS), NEB, and NTB; (2) organized folded filamentary regions (size 15000 km, filament width  $\sim 600$  km); (3) elongated areas with contours closed by a ribbon-like feature; (4) discrete brown elongated ovals called “barges” (zonal extent  $\sim 5000$  km). Hatzes *et al.* (1981) measured the peripheral circulation of a barge and its shape oscillations. Like the cyclonic belts, the closed cyclonic features are warmer than their surroundings at upper tropospheric levels, consistent with downwelling (Conrath *et al.* 1981).

At some latitudes the anticyclones “invade” the belt on their equatorward side and break it into a series of closed cyclonic cells. The cyclones alternate in longitude with the anticyclones, but they are offset from each other in latitude. This alternating pattern resembles a classic Karman vortex street (Youssef and Marcus 2003). In the laboratory and in nature, such configurations form in wakes behind blunt bodies and are stable to small perturbations. On Jupiter there is an asymmetry between the anticyclones and cyclones: The former are more compact; the latter are more elongated and have a more chaotic texture. For example, the 12 compact anticyclonic white ovals at  $41^\circ\text{S}$  alternate in longitude with chaotic cyclonic patches that are a few degrees closer to the equator than the anticyclonic ovals (Figure 6.5, left). Such an asymmetry is not present in a classic vortex street but could arise in a rotating planetary atmosphere, perhaps because the anticyclones are vertically thicker, which follows from the thermal wind equation, or perhaps because the cyclonic belts are the sites of moist convection.

### 6.3.4 Eddy Momentum Flux

The word “eddy” refers to all the non-zonal features – the residuals after subtracting off the zonal mean (average with respect to longitude). Eddy winds  $u'$  and  $v'$  are the residual eastward and northward velocity components after subtracting off the means  $\bar{u}$  and  $\bar{v}$  for that particular latitude band. The covariance  $\overline{\rho u'v'}$  is the northward eddy flux of eastward momentum and is an important diagnostic of the flow. The eddy heat flux  $\rho C_p \overline{v'T'}$  has never been measured, and the values of  $\bar{v}$  are smaller than the measurement error.

Beebe *et al.* (1980) and Ingersoll *et al.* (1981) used a data set containing over 14 000 individual velocity vectors to determine  $\overline{\rho u'v'}$  for 120 latitude bands, each  $1^\circ$  wide, from  $60^\circ\text{S}$  to  $60^\circ\text{N}$ . They found that the sign of the eddy momentum flux depends on the sign of  $d\bar{u}/dy$ , where  $y$  is the northward coordinate. At latitudes where  $d\bar{u}/dy$  is positive the eddy momentum flux tends to be positive, and vice versa (Beebe *et al.* 1980, Ingersoll *et al.* 1981). Figure 6.11 shows  $d\bar{u}/dy$  and the correlation coefficients  $r(u',v')$  from *Voyagers 1* and *2*, all as functions of latitude. The data refer to cloud-top levels, 0.7 to 1.0 bars. The fact that the three curves show in-phase variations indicates that the eddy momentum flux is *into* the jets, which is opposite to what one would expect from turbulent diffusion. This up-gradient momentum transfer occurs in the terrestrial jet streams as well, but the ratio of energy transfer into the jets to the power radiated by the planet is only  $\sim 0.001$ . On Jupiter the

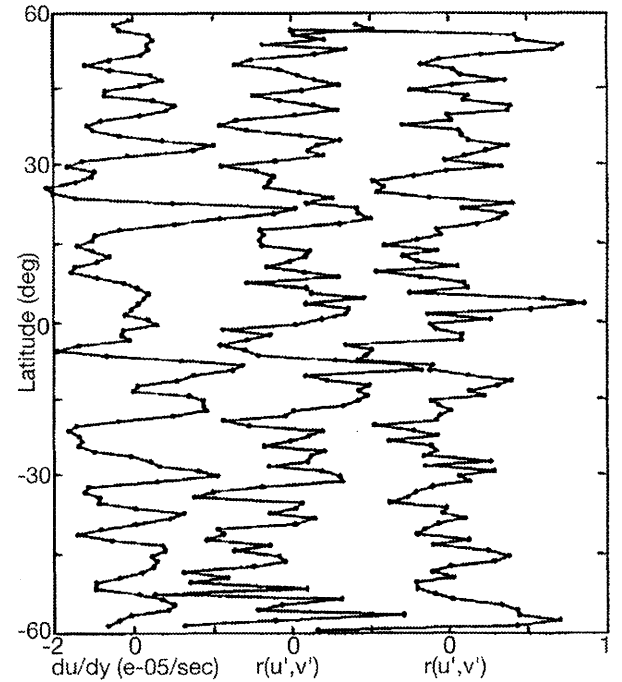


**Figure 6.11.** Zonal velocity gradient  $d\bar{u}/dy$  (left) and the correlation coefficient  $r(u',v')$  from *Voyager 1* (center) and *Voyager 2* (right), from Ingersoll *et al.* (1981). Here  $u'$  and  $v'$  are the eastward and northward velocity components after subtracting the mean winds. The similarity of the three curves as a function of latitude indicates that the correlation between the components is significant. The fact that the correlation tends to have the same sign as  $d\bar{u}/dy$  indicates that the eddy momentum transport is into the jets and tending to accelerate them.

ratio is  $\sim 0.1$ , assuming the energy transfer is taking place in a layer 2.5 bars thick, e.g., from the 0.5-bar level to the 3.0-bar level (Ingersoll *et al.* 1981). The ratios are a measure of power in the mechanical energy cycle compared to that in the thermal energy cycle, and seem to imply that the jovian heat engine is much more efficient than the Earth's. Up-gradient transfers do not violate physical laws as long as the eddies have a source of energy that is separate from the shear flow. Buoyancy-driven convection is an obvious energy source that operates on both Earth and Jupiter.

Sromovsky *et al.* (1982) challenged this estimate of the eddy momentum flux. They correctly pointed out that biases could arise in measuring the 14 000 velocity vectors. A human operator had to choose a cloud feature and find it in a second image taken at a different time. This target-of-opportunity approach does not sample the planet uniformly. A spurious signal could arise, for example, if there were more features on the SE and NW sides of a large vortex and fewer on the SW and NE sides. Clearly the procedure needs to be automated and the measurement of  $\overline{\rho u'v'}$  needs to be re-done.

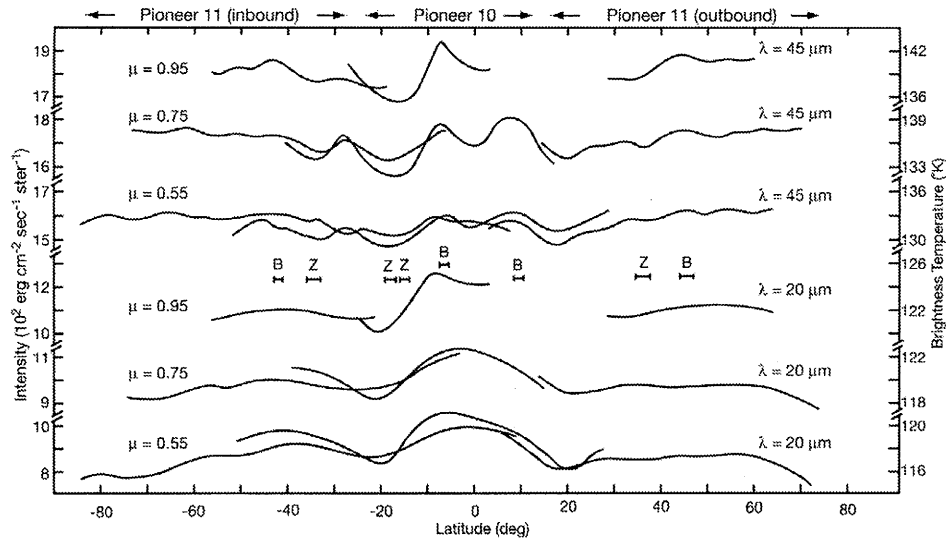


**Figure 6.12.** Brightness temperature (right-hand ordinate) and intensity (left-hand ordinate) as a function of latitude for three different values of the emission angle cosine (Ingersoll *et al.* 1976) at wavelength bands centered at 20 and 45  $\mu\text{m}$ . The data are from *Pioneer 10*, which viewed the low latitudes, and *Pioneer 11*, which reached higher latitudes than any other spacecraft. Significant features of the curves include: (1) the agreement between *Pioneers 10* and *11*, (2) the lack of pronounced equator-to-pole contrasts, and (3) the higher brightness temperatures in belts (B) compared to zones (Z).

## 6.4 TEMPERATURES AND VERTICAL STRUCTURE

### 6.4.1 Global Temperature Variations

As shown in Figure 6.12, Jupiter has no appreciable equator-to-pole temperature gradient (Ingersoll *et al.* 1976, Pirraglia 1984). Except for variations on the scale of the belts and zones, the emitted infrared radiation is independent of latitude. This means that energy is being transported poleward, either in the atmosphere or in the interior, to make up for the extra sunlight absorbed at the equator. Ingersoll (1976a) and Ingersoll and Porco (1978) argued that Jupiter's internal heat flux is diverted poleward by slightly lower polar temperatures at the top of the convection zone. Deep convection acts as a thermostat that maintains the equator and poles at essentially the same temperature. The fluid interior short-circuits the atmosphere, they argued, leaving it with no role in the global energy budget. Earth's oceans cannot do this because they are heated from above and are therefore dynamically less active than the atmosphere.

Jupiter has seasons despite its low  $3^\circ$  obliquity. Orton *et al.* (1994) found high-latitude temperature maxima two years after solstice at the 250-mbar level. The data cover one jovian year, from 1979 to 1993. This phase lag is consistent with the computed radiative time constant, which has a minimum of  $4 \times 10^7$  s at the tropopause (Flasar 1989).

A prominent non-seasonal variation occurs in the Equatorial Zone (EZ), whose 250-mbar temperature oscillates with a 4-year period and appears to be opposite in phase with the 20-mbar temperature (Orton *et al.* 1991, Chapter 7). Leovy *et al.* (1991) termed this the quasi-quadrennial oscillation (QQO) of Jupiter, and related it to upward-propagating, equatorially trapped waves in analogy with the quasi-biennial oscillation (QBO) of Earth's tropical atmosphere. Using a numerical model, Friedson (1999) showed that large-scale equatorial waves are ineffective in driving

the oscillation but that forcing by small-scale gravity waves provides a better fit to the observations (cf. Li and Read 2000).

Orton *et al.* (1994) also noted a large cooling at the 250-mbar level from 1985 to 1990 in a region between approximately  $15^\circ\text{N}$  and  $27^\circ\text{N}$  (planetocentric), i.e., between the northern boundary of the NEB and the northern boundary of the North Temperate Belt (NTB). They estimated that if winds were steady at the cloud-top level near 600–700 mbar then a large cooling trend at the 250-mbar level recorded between 1985 and 1990 implied, through the thermal wind relationship, that the zonal wind decreased by at least  $3 \text{ m s}^{-1}$  per terrestrial year.

### 6.4.2 Thermal Waves

The profiles of the *Voyager* radio occultation experiment (Lindal *et al.* 1981) show wave-like features (Figure 6.13), although Lindal *et al.* suggested that they could be the result of local particulate layers that absorb sunlight. The features have vertical length scales of  $\sim 1.5$  pressure scale heights and amplitudes of 5–25 K. The horizontal structure is unknown, as is the wave period. Vertical waves are evident in the *Galileo* probe measurements of Jupiter's temperature structure (Seiff *et al.* 1998). Stellar occultation results showing temperature oscillations in the upper stratosphere reinforce the wave interpretation of the *Galileo* probe results.

Longitudinally varying thermal features that do not correlate with visible features have been observed in the upper troposphere (Magalhães *et al.* 1989, Deming *et al.* 1989, 1997, Fisher 1994, Orton *et al.* 1994, Harrington *et al.* 1996). The amplitude is largest over the NEB and SEB, but is also evident in belts farther from the equator. The waves are essentially stationary relative to System III, independent of cloud-tracked winds at the same latitude. Power spectra of these oscillations show that longitudinal wavenumbers less

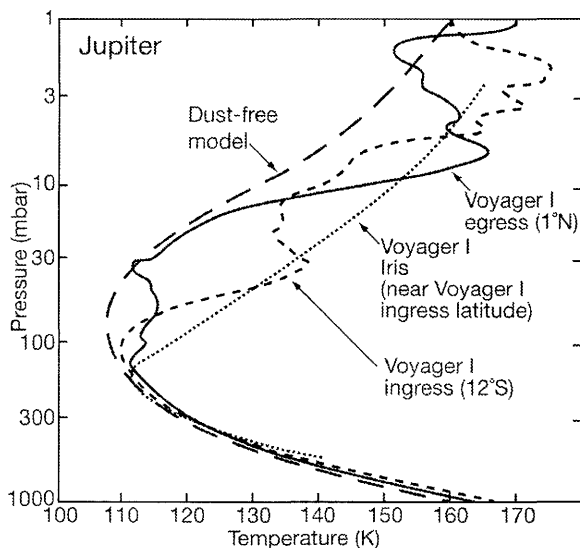


**Figure 6.13.** Temperatures in the upper troposphere and stratosphere (Lindal *et al.* 1981). The *Voyager 1* ingress and egress curves are from the radio occultation experiment and are for specific points on the planet. They show large-amplitude wave-like features. The *Voyager 1* IRIS curve is an inversion of radiance data and covers a much wider area than the occultation profiles. The dust-free model assumes radiative equilibrium above the temperature minimum and does not take into account possible dust particles that might absorb sunlight and heat the atmosphere.

than 15 predominate (Deming *et al.* 1997, Orton *et al.* 1998, Fisher *et al.* 2001). These features are widely assumed to be vertically propagating Rossby waves (e.g., Deming *et al.* 1997, Friedson 1999, Li and Read 2000). Fundamentals of the phenomenon, such as how they are forced and whether they are exactly fixed to System III are not known.

#### 6.4.3 Vertical Structure – Winds

The *Galileo* probe measured the zonal wind profile from the 0.5-bar pressure level down to the 22-bar level (Atkinson *et al.* 1998). The measurement was supposed to settle the question of whether the winds are shallow or deep (Section 6.2.4). The general expectation was that the winds would either decrease to zero at the base of the water cloud or would be constant with depth. In fact the winds *increased* with depth from 1 to 4 bars and then remained constant (Figure 6.14). Clearly the winds are not confined to the altitudes above the water cloud base at 6- to 7-bars. In that sense, the winds are “deep,” but the interpretation is complicated by the local meteorology of the probe entry site.

Winds are related to temperatures through the thermal wind equation. A barotropic fluid has constant temperature on constant-pressure surfaces, and the winds are constant with depth. If the fluid is not barotropic it is referred to as baroclinic, and the winds vary with depth. A single temperature profile, like the one derived from the *Galileo* probe, cannot distinguish between a barotropic and a baroclinic state. But if the flow is baroclinic, there must be gradients of potential temperature (gradients of specific entropy). Therefore a layer that is stably stratified, with potential temperature increasing with altitude, is more likely to be baroclinic.

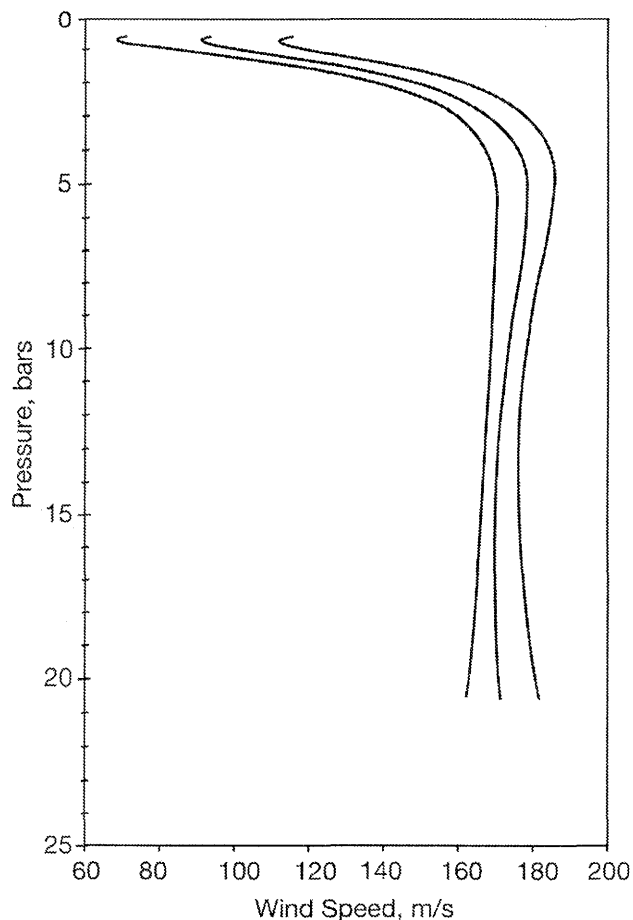


**Figure 6.14.** Eastward wind *vs.* altitude measured by the Doppler wind experiment on the *Galileo* probe (Atkinson *et al.* 1998). The three curves show the range of acceptable solutions. The 100 m s<sup>-1</sup> speed at the 0.7-bar level agrees with the cloud-tracked wind speed at this latitude (6.5°N).

Conversely, a layer that is neutrally stratified (dry adiabatic, i.e., potential temperature constant with altitude) is more likely to be barotropic. In other words, a stably stratified layer acts to decouple the winds above from the winds below.

The wind profile measured by the probe is at least consistent with this picture: The wind varied with depth (baroclinic behavior) inside the clouds in the 1- to 4-bar range where moist convection is expected to produce potential temperature gradients, and the wind remained constant with depth (barotropic behavior) below the clouds where dry convection is expected to eliminate the potential temperature gradients. A problem with this picture is that the measured temperatures followed a dry adiabat more closely than a moist adiabat in the 1- to 4-bar region, but that may be a special property of 5- $\mu$ m hot spots.

#### 6.4.4 Vertical Structure – Temperature

The *Voyager* radio occultation results (Lindal *et al.* 1981) reveal a statically stable atmosphere above 300 mbar and a dry adiabat near 1 bar (Figure 6.13). The bulk of Jupiter's interior is expected to be convective, and the simplest model

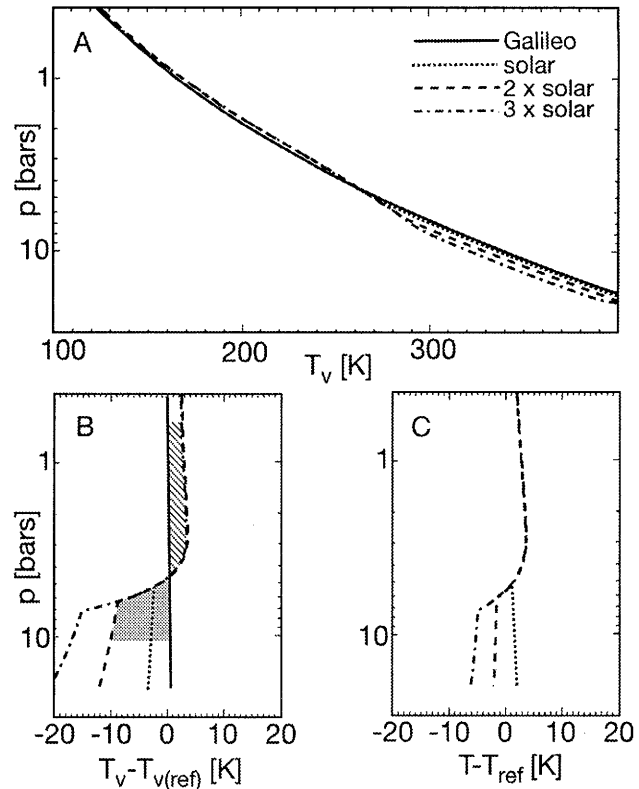
is one where the atmosphere follows a dry adiabat from the interior up to the base of the water cloud and a moist adiabat within the cloud. The latter is indistinguishable from a dry adiabat near 1 bar where latent heat effects are negligible. This picture seems to work in the Earth's tropics, where the atmosphere over the ocean is close to moist adiabatic.

Figure 6.15, from Showman and Ingersoll (1998), shows a comparison between moist and dry adiabats for three cases, in which the deep abundance of water is 1, 2, and 3 times solar (elemental abundance ratios equal to those on the Sun). Ammonia and  $\text{H}_2\text{S}$  are assumed to be solar, and their effects on the latent heat release and molecular mass are included. Virtual temperature  $T_V$  is related to buoyancy and is defined as  $Tm_0/m$ , where  $m_0$  is the molecular mass of dry air and  $m$  is molecular mass of the mixture – dry air plus condensable vapor. As pressure decreases,  $T_V$  increases relative to the dry adiabat, both because latent heat is released and because the heavier condensate falls out. The effect of water can easily exceed 10 K, and the associated static stability (virtual temperature gradient minus the adiabatic gradient) is large. The effect of ammonia and  $\text{H}_2\text{S}$  are only several times 0.1 K, largely because these gases are less abundant and also because their latent heats are smaller (Atreya 1986). Numerical simulations that explicitly model the interaction between convection and condensation in the 1- to 10-bar layer give the same result – a statically stable layer at a few bars that is overlain and underlain by neutrally stable layers (Nakajima *et al.* 2000).

The *Galileo* probe found a temperature profile that was close to dry adiabatic at all levels below 1 bar (Seiff *et al.* 1998). Using the probe data, Magalhães *et al.* (2002) derive a small static stability that varies between 0 and  $0.2 \text{ K km}^{-1}$  in the 1- to 22-bar region. The measurement uncertainty is  $\sim 0.1 \text{ K km}^{-1}$ . Inferences based on a gravity wave interpretation of the probe's vertical motion (Allison and Atkinson 2001) are generally consistent with this result. For comparison, if Jupiter's atmosphere were isothermal the static stability would be  $\sim 2 \text{ K km}^{-1}$ , and if the water abundance were 1–3 times solar the static stability, defined by the difference in  $T_V$  between moist and dry adiabats (Figure 6.15), would be  $\sim 1 \text{ K km}^{-1}$ .

To infer the static stability away from the probe site, one relies on indirect methods, which do not always agree. Several types of waves that require a stable layer to propagate have been observed. Mesoscale waves with  $\sim 300 \text{ km}$  horizontal wavelength are seen in *Voyager* and *Galileo* images. Bosak and Ingersoll (2002) suggest they are an example of shear instability in a layer of small static stability. Flasar and Gierasch (1986) suggest they are ducted gravity waves in a sub-cloud layer of large static stability. Such a statically stable layer would help to explain the existence of the equatorial plumes (Allison 1990). And narrow, expanding rings observed after the collision of Comet Shoemaker-Levy 9 with Jupiter (Hammel *et al.* 1995) have been interpreted as the stratospheric tails of gravity waves ducted by a stable layer below the clouds (Ingersoll and Kanamori 1995). It is possible that the SL9 waves can be explained without the tropospheric stable layer (Walterscheid *et al.* 2000). If the Ingersoll and Kanamori (1995) interpretation is correct, and if the stable layer results from latent heat release, then the water abundance must be  $\sim 10$  times solar.

Dynamical models that include a statically stable layer



**Figure 6.15.** Temperatures computed for an atmosphere with 1, 2, and 3 times solar abundances of  $\text{H}_2\text{O}$ . The abundances of  $\text{NH}_3$  and  $\text{H}_2\text{S}$  are solar in each case. The dashed lines show the temperature along the three moist adiabats, all of which pass through the point 169 K at 1 bar as measured from the *Voyager* radio occultation (Lindal *et al.* 1981). The solid line is the profile measured by the *Galileo* probe (Seiff *et al.* 1998). Buoyancy is measured by virtual temperature  $T_V$ , which includes the effects of both physical temperature and molecular mass of the condensate. (A)  $T_V$  vs.  $\log P$ . (B) The same, but with the dry adiabat subtracted. (C) Temperature  $T$  vs.  $\log P$  with the dry adiabat subtracted (Showman and Ingersoll 1998).

near the clouds have been generally successful in explaining the basic features of Jupiter's jets and vortices (e.g., Dowling and Ingersoll 1989, Cho and Polvani 1996, Achterberg and Ingersoll 1989, 1994, Williams 1996, Marcus and Lee 1998, Showman and Dowling 2000, Cho *et al.* 2001). The deformation radius  $L_d$ , which is the distance beyond which two vortices do not interact, is estimated to be  $\sim 2000 \text{ km}$  within a factor of about two.  $L_d$  is related to the static stability of the atmosphere, and the 2000 km value is roughly consistent with the stabilities expected from the moist-convection and wave considerations listed above. However, the large-scale dynamics models are not yet detailed enough for a definitive comparison.

Showman and Ingersoll (1998) point out that the decrease of probe-derived wind speed with altitude in the 1- to 4-bar pressure range implies substantial gradients of temperature with latitude, and that these gradients change with height. This condition requires that the probe site be stably stratified from 1- to 4-bars, with a total stability of order 1 K; otherwise, regions near the probe site would be statically unstable, which is unphysical. The inferred  $\sim 1 \text{ K}$

stability between 1 and 4 bars at the probe site is consistent with the recent probe analyses of Magalhães *et al.* (2002).

The static stability measured by the probe is less than that suggested by the pre-*Galileo* wave-duct and moist-convection arguments. Showman and Dowling (2000) and Friedson and Orton (1999) point out, however, that hot spots are probably the troughs of a large-scale wave, in which columns of air have been forced down and vertically stretched by a factor of several. This mechanism would decrease the mean static stability and push the high static stability region associated with the water condensation level (which was originally near 7 bars, Figure 6.15) down to pressures greater than 22 bars, deeper than observed by the probe (Showman and Ingersoll 1998). The low static stabilities measured by the probe are therefore perhaps not representative of Jupiter as a whole.

## 6.5 MOIST CONVECTION AND LIGHTNING

### 6.5.1 Lightning Distribution

*Voyager*, *Galileo*, and *Cassini* detected lightning in long-exposure images of Jupiter's nightside (Borucki and Magalhães 1992, Little *et al.* 1999, Gierasch *et al.* 2000, Porco *et al.* 2003). The lightning strikes were concentrated in clusters, suggesting that several discrete storms produced multiple strikes during each of the exposures. Twenty-six unique storms were documented in the two *Galileo* data sets. The locations of lightning clusters have been correlated with the locations of small, bright clouds on dayside images. Although data are scarce, these thunderstorm clusters appear to be associated with high levels of humidity (Roos-Serote *et al.* 2000) and clouds at deep levels where water would be expected to condense (Banfield *et al.* 1998).

As shown in Figure 6.16, lightning-bearing storms appear to be concentrated within narrow latitudinal bands that are related to Jupiter's zonal jet structure. In fact, every storm occurs within a region of cyclonic shear or the neighboring westward jet, and 10 of the 11 regions of cyclonic shear (belts) equatorward of  $\pm 60^\circ$  latitude are known to contain lightning storms. Belts near  $47^\circ\text{N}$  and  $52^\circ\text{S}$  produced significantly more lightning strikes per area than other belts. Finally, *Galileo*'s probe detected radio emissions that can be explained by a lightning-like source about  $12^\circ$  from the probe site, which was at  $6.54^\circ\text{N}$  PG latitude (Rinnert *et al.* 1998).

### 6.5.2 Convective Heat Flux and Structure of the Lightning Clouds

In May 1999, *Galileo* took time-lapse images of the SEB on the dayside followed by lightning searches on the nightside two hours later. Two lightning storms were found (Gierasch *et al.* 2000). Figure 6.17 displays a false color image revealing optically thick clouds at high elevation within a few hundred kilometers of a deep cloud, located where the nightside images showed lightning flashes. Radiative modeling (Banfield *et al.* 1998) of methane band and continuum images places the high cloud at a pressure of a few hundred mbar and the deep cloud at a pressure exceeding 3 bars, where water is the only possible condensate. The authors conclude

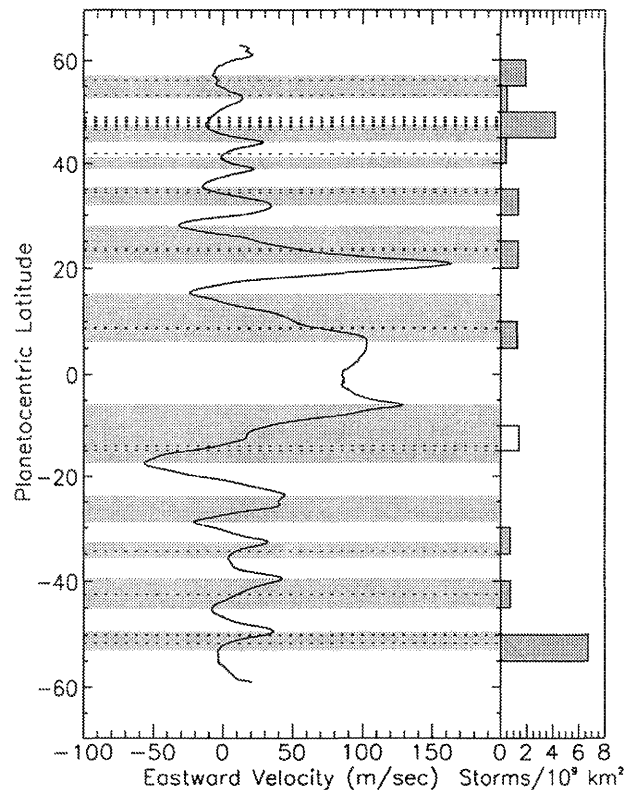


**Figure 6.16.** Latitude of lightning storms (horizontal lines) observed in *Galileo* nightside images compared to the zonal velocity profile (Limaye 1986). The bars on the right show the number of lightning storms per unit area in latitude bins  $5^\circ$  wide. Most of the observations are from a broad survey that covered more than half the planet in late 1997 (Little *et al.* 1999). The observations near  $15^\circ\text{S}$  are from an intensive study of the SEB in mid-1999 (Gierasch *et al.* 2000). Lightning storms predominate in the cyclonic bands, where the velocity is decreasing (increasing) with latitude in the northern (southern) hemisphere.

that moist convection involving water is occurring. Velocity vectors show divergence within the high cloud over one of the storm centers, consistent with termination of an updraft. Near-infrared observations of the NEB (Roos-Serote *et al.* 2000) showed high concentrations of water vapor in the vicinity of one of these high, thick clouds. In this case there was no nightside imaging, so it was not possible to confirm that this was a lightning storm.

Both the lightning and the small, intense, rapidly diverging storms are observed almost exclusively in the belts. It is possible that this is an observational effect – that the uniform high clouds of the zones are covering convective activity below, but this possibility is unlikely for two reasons. First, the small intense storms penetrate to higher levels than the uniform clouds in the zones, and therefore should be visible if they were present there. Second, the photons from the lightning seem able to reach the surface from great depths through optically thick clouds. They too should be visible in the zones if they were present.

Gierasch *et al.* (2000) estimate that the lightning storms are carrying most of the planet's internal heat flux. They base their estimate on (1) the temperature difference ( $\sim 5\text{ K}$ ) between the atmosphere at the top of the convective clouds and the adiabat from the deep interior, (2) the vertical mass

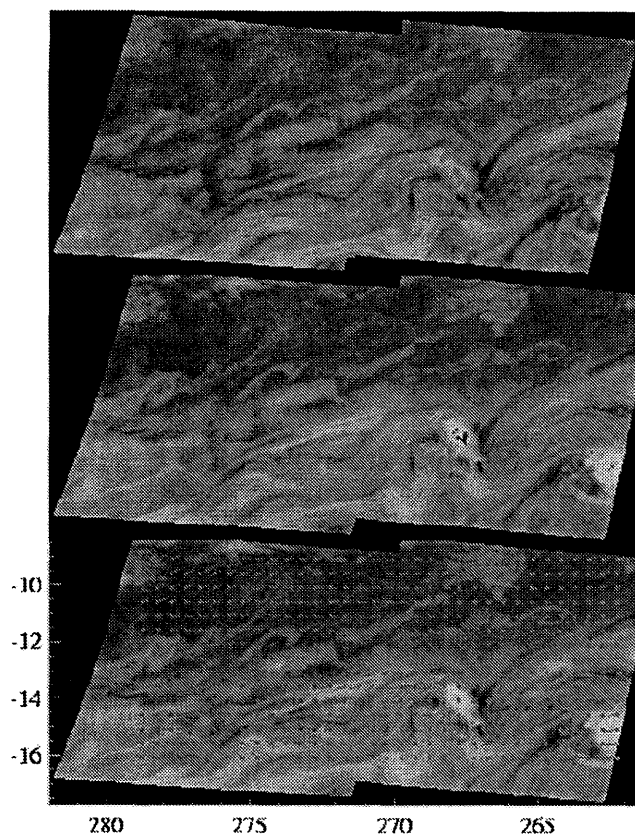


**Figure 6.17.** Lightning storms (Gierasch *et al.* 2000) in the southern hemisphere. The top panel is a superposition of a continuum wavelength (756 nm) in the red plane, a medium methane band (727 nm) in the green plane, and a strong methane band (889 nm) in the blue plane. The location of lightning is shown by the blue overlay on to a continuum image in the middle panel. Note the close proximity of red (deep) features and bright white (high) features to the flash locations. The bottom panel shows velocity vectors derived from three time-steps in the continuum. The flags point downwind, and the largest flag corresponds to a speed of  $70 \text{ m s}^{-1}$ . The large-scale flow structure is eastward near the top of the frame (the north edge) and westward near the bottom. In the southern hemisphere this represents cyclonic shear. Approximate latitude and longitude are indicated on the bottom panel. This region is  $\sim 30^\circ$  west of the Great Red Spot. At the time of going to press a colour version of this figure was available for download from <http://www.cambridge.org/9780521035453>.

transport, which they get from the rate of horizontal divergence, and (3) the number of convective storms per unit surface area. The latter estimate comes from earlier *Galileo* observations that surveyed most of the planet's surface for lightning (Little *et al.* 1999).

### 6.5.3 Energy of Lightning Flashes

The measurable quantities are optical energy per flash and average optical power per unit area. Flash rate and color are measurable in principle. The optical range is here defined by the transmission of the *Galileo* clear filter, which goes from 385 nm to 935 nm (Little *et al.* 1999). One assumes that the photons are emitted uniformly in all directions. This gives a lower bound on the energy because clouds above the flash site may scatter the photons back down where they are absorbed.

Jovian lightning occurs in storms whose sizes range from 200 km to over 1000 km and whose separation distance is  $\sim 10^4$  km (Little *et al.* 1999). A 1-min exposure captures 10–20 flashes, which therefore overlap in the image. Overlap is not a problem if one is calculating the average optical power of the storm, but it prevents one from estimating the properties of individual flashes. Fortunately, the *Galileo* camera captured three lightning storms in a “scanned” frame – a 59.8 s exposure that was deliberately smeared across the disk so that each storm left a trail of bright dots where the individual flashes occurred. The brightest flash in the scanned frame was  $1.6 \times 10^{10}$  J (Little *et al.* 1999). This is three times brighter than the largest terrestrial superbolts (Borucki *et al.* 1982). Smaller flashes are more numerous, but most of the storms' optical energy is carried in the largest flashes. The detection threshold for the *Galileo* and *Voyager* cameras is about  $2 \times 10^8$  J, which is larger than the average terrestrial flash. Thus it is not possible to compare the global flash rates (number of flashes per unit area per unit time). However the average optical power per unit area is about the same for Earth and Jupiter,  $3\text{--}4 \times 10^{-7} \text{ W m}^{-2}$ , even though the convective heat fluxes differ by more than an order of magnitude ( $\sim 80 \text{ W m}^{-2}$  for Earth *vs.*  $\sim 6 \text{ W m}^{-2}$  for Jupiter) and the hydrologic cycles are fundamentally different.

The spectral energy density ( $\text{W nm}^{-1}$ ) measured by *Galileo* was greatest in the red filter, next greatest in violet, and least in green. The *Cassini* H $\alpha$  filter (centered on a strong line of atomic hydrogen at 656 nm) had the highest spectral energy density of all. While these results are consistent with a mixture of line and continuum emission in a hydrogen–helium atmosphere (Borucki *et al.* 1996), it is difficult to infer physical properties of the lightning (discharge rate, temperature, or pressure) from these data alone.

### 6.5.4 Depth of Lightning

Since the photons are diffusing up through the intervening clouds, the depth of the lightning is roughly proportional to the width of the bright spot in the image. Width is defined as the half-width at half-maximum (HWHM), the radius of the circle where the intensity is one-half the value at the center of the spot. Scattering models put the ratio depth/HWHM in the range 1–2 (Borucki and Williams 1986, Little *et al.* 1999, Dyudina *et al.* 2002). The difficulty is finding lightning flashes that are well resolved (pixel size  $\leq 25$  km), not overlapped, and not saturated.

Borucki and Williams (1986) report that the average HWHM for lightning observed in the *Voyager* images is  $55 \pm 15$  km. The HWHMs for six *Galileo* flashes are 87, 69, 37, 72, 42, and 50 km (Little *et al.* 1999, Dyudina *et al.* 2002). This puts the average depth in the range 60–120 km, depending on the parameters of the scattering model. The largest flashes could be even deeper.

With these large depths the lightning could be below the freezing level or even below the base of the water cloud, unless the water abundance is much higher than implied by solar values of the O/H ratio. The radiative properties of the clouds introduce a large (factor of 2) uncertainty. Not only are the radiative properties uncertain, but the shape of the clouds are uncertain and are apparently not plane-parallel. Optical depth is greatest over the lightning and falls off with

horizontal distance (Dyudina *et al.* 2002). There is a small possibility that some of the flashes are doubles. Nevertheless, the conclusion is that the lightning flashes are deep – that they must be occurring within or below the jovian water cloud (Little *et al.* 1999).

### 6.5.5 Models of Moist Convection

Conrath and Gierasch (1984) discussed the relative buoyancy effects of latent heat release, hydrogen ortho–para conversion, and molecular weight differentiation on the outer planets and found that all three are in principle capable of causing density perturbations on the order of 1%. Smith and Gierasch (1995) showed that ortho–para effects are less important for Jupiter than they are for Uranus and Neptune. Detailed modeling of moist buoyancy effects on Jupiter, with the environment (in which the plume is imbedded) fixed by initial conditions, yielded updraft velocities as high as tens of  $\text{m s}^{-1}$  (Stoker 1986, Lunine and Hunten 1987). Self-consistent convective adjustment experiments (Delgenio and McGrattan 1990) gave layered profiles in the vertical and a subsaturated, stably stratified mean state.

Convective adjustment predicts mean profiles but not detailed flow fields, which are necessary eventually to explain charge separation and lightning. Yair *et al.* (1995, 1998) use an axisymmetric numerical flow model to study examples of moist convection. Hueso and Sánchez-Lavega (2001) and Hueso *et al.* (2002) developed a three-dimensional numerical model of moist convective storms that include vertical wind shears. Again an environmental stratification and specific initial conditions are imposed. These authors obtain flows consistent with precipitation and lightning when sufficient water vapor is introduced ( $\text{O}/\text{H} \geq \text{solar}$ ) and low stability is assumed.

The fact that lightning storms and moist convection seem to occur in the cyclonic belts needs an explanation, particularly since the air in the belts is sinking, at least in the upper troposphere. On Earth moist convection is associated with low-level convergence and rising motion. One possibility is that the air in the belts is rising in the lower troposphere, with horizontal divergence at intermediate levels (Ingersoll *et al.* 2000). Such divergent flow might be driven by the eddy flux  $\overline{\rho u'v'}$ , which accelerates the jets on either side of the belt. Balancing the eddy acceleration of an eastward (westward) jet requires transport of low (high) angular momentum air from higher (lower) latitudes. Since the eastward jets are on the equatorward sides of the belts and the poleward sides of zones, the net result is horizontal divergence in the belts and horizontal convergence in the zones. The updraft in the lower troposphere beneath the belts brings water vapor up from the interior and leads to moist convection.

## 6.6 MODELS OF THE ZONAL JETS

### 6.6.1 Banding Controlled in the Weather Layer

Two length scales have been invoked to explain the widths of the zonal jets. The first is the deformation radius  $L_d = NH/|f|$ , where  $N$  is the Brunt–Väisälä frequency (the buoyancy frequency),  $H$  is the pressure scale height ( $\approx$ vertical

scale of motion), and  $f = 2\Omega \sin(\phi)$  with  $\Omega$  the planet's angular velocity and  $\phi$  the latitude (e.g., Pedlosky 1987). Attributed to Rossby,  $L_d$  is the horizontal distance beyond which two vortices do not strongly interact. Alternatively, it is the maximum size of features for which the fluid is barotropic and vertical stretching of vortex tubes is negligible. The deformation radius is relevant where  $f \neq 0$ , i.e., away from the equator. If there is a stable layer associated with moist convection within the water cloud (Achterberg and Ingersoll 1989, Ingersoll and Kanamori 1995), then  $L_d$  may be written  $c/|f|$  where  $c$  is the speed of gravity waves that are ducted in the layer. Its value is estimated to be  $\sim 2000$  km in Jupiter's troposphere at mid latitudes, with both the uncertainty and the natural variability probably a factor of 2 in each direction. The value of  $L_d$  could be much smaller if the low values of  $N$  measured by the *Galileo* probe are typical of the planet as a whole.

The second length scale is  $L_\beta = (U/\beta)^{1/2}$ , where  $U$  is the magnitude of the horizontal velocity,  $\beta \equiv df/dy = 2\Omega \cos(\phi)/a$  is the planetary vorticity gradient, and  $a$  is the planetary radius. Attributed to Rhines, it is the scale above which the speed of a barotropic Rossby wave is greater than the wind speed. Alternatively, it is the critical width of the zonal jets below which they might be unstable. The barotropic stability criterion says that the flow is stable provided  $Q_y \equiv \beta - \bar{u}_{yy} > 0$  at all latitudes, where the subscripts denote differentiation with respect to  $y$ . Here  $Q_y$  is the absolute vorticity gradient, the sum of the planetary vorticity gradient  $\beta$  and the relative vorticity gradient  $-\bar{u}_{yy}$ . *Voyager* data imply that  $\bar{u}_{yy}$  varies between  $\pm 2\beta$  and therefore that the criterion is violated (Ingersoll *et al.* 1981, Limaye 1986). Reproducing this observation is a major challenge for the models. One possibility is that the variation of wind with altitude, which is ignored in barotropic models, is affecting the stability of the flow.

Rhines (1975) demonstrated that zonal jets emerge from decaying turbulence on a  $\beta$ -plane – a planar coordinate system that preserves the important effects of the planet's curvature and rotation. Williams (1978) first applied these ideas to Jupiter. These  $\beta$ -turbulence models have some common features. First, they describe motion in a thin layer, either on a  $\beta$ -plane or on the surface of a sphere; motions in the planet's interior are neglected. Second, they rely on small-scale forcing. The classic inverse cascade models (Vallis and Maltrud 1993, Huang and Robinson 1998, Marcus *et al.* 2000, Sukoriansky *et al.* 2002) have positive and negative sources of vorticity at small scales. The baroclinic models (Panetta 1993) have an unstable temperature gradient that produces eddies at the  $L_d$  scale. Other models (Williams 1978, Cho and Polvani 1996) start with an initial eddy field that evolves without dissipation to a set of zonal jets. There is a strong anisotropy between the zonal and meridional directions; zonal jets develop in all the models. But in all cases the resulting jets have  $\bar{u}_{yy} < \beta$ ; they are too wide and too weak to violate the barotropic stability criterion and therefore do not fully agree with the Jupiter data.

Another mystery is why Jupiter has weaker winds than any other giant planet despite its greater radiative energy fluxes – absorbed and emitted power per unit area. For example, Neptune's winds are  $\sim 3$  times stronger than Jupiter's, but the radiative fluxes at Neptune are  $\sim 20$  times weaker. One possibility (Ingersoll 1990, Ingersoll *et al.* 1995)

is that the radiative fluxes determine the level of atmospheric turbulence, which dissipates the energy of the large-scale winds. If the turbulence levels decrease by a large amount as the radiative fluxes decrease, and the energy sources that drive the winds decrease by a smaller amount, the large-scale winds would increase. By this token, the high-speed jets of Neptune are coasting in an atmosphere where dissipation is low. Jupiter's atmosphere is more turbulent, which limits the speed of the large-scale winds. Interestingly, Earth has the weakest large-scale winds and the strongest radiative heating of any atmosphere-covered planet in the solar system.

### 6.6.2 Deep Winds and Stability of the Jets

Jupiter's strong, narrow jets are unstable if one assumes that the winds are confined to a thin horizontal layer. For instance, Dowling and Ingersoll (1989) showed that Jupiter's cloud-top winds suffer barotropic instability and evolve away from what is observed when initialized in a shallow-water model with no deep circulation. However, Ingersoll and Cuong (1981) found that the upper-layer wind profile is stable if it rests hydrostatically on a co-moving deep lower layer whose density is greater than that of the upper layer. This is an extension of the idea that the observed zonal jets are the surface manifestation of differentially rotating cylinders concentric with the planet's rotation axis (Busse 1976). Ingersoll and Pollard (1982) showed that the rotating cylinders could be stable even though they violate the barotropic stability criterion because that criterion applies only to motions in thin shells. They developed a criterion that applies to motions inside a compressible fluid sphere, where the effective  $\beta$  is negative and is 2 or 3 times larger than the traditional  $\beta$ . Jupiter's observed winds are closer to marginal stability according to this criterion. However, the rotating cylinders penetrate into the interior where the electrical conductivity is high and the magnetic field may interfere with the flow (Kirk and Stevenson 1987). A complete theory would take these hydromagnetic effects into account.

Orsolini and Leovy (1993a, 1993b) examined the linear instability problem in cases where there is a deep circulation, to see whether the motions in the overlying atmosphere can be stabilized. They found that jets that decay with height are more stable than those that do not. This agrees with work by Pirraglia (1989) and is consistent with the jet decay with height inferred for Jupiter via the thermal-wind analysis. These two studies demonstrate the potential importance of the deep flow for the stability of the jets, but they do not discuss how the deep flow is maintained.

Dowling and Ingersoll (1988, 1989) deduced the nature of the deep circulation by observing changes in absolute vorticity as parcels move around the GRS and white oval BC. Changes in absolute vorticity are due to vortex tube stretching, which arises when the parcels cross the pressure ridges associated with the flow underneath. The analysis produced a family of possible deep circulations with  $L_d^2$  as the unknown scaling factor. For each case, the deep flow is not in solid rotation; it seems to have a jet-like structure somewhat like that observed in the upper layer. Dowling (1993) showed that this family of abyssal circulations corresponds to the special case  $L_d = L_\beta$ , where  $\beta$  is the full gradient of potential vorticity including the vertical stretching term.

This condition corresponds to the case of marginal stability with respect to a criterion that traces back to Kelvin and is now known as Arnol'd's second stability criterion (although it is notably absent from most meteorology textbooks). It allows a shear flow to be stable even though the flow does not satisfy other, better-known stability conditions. Here again, the abyssal circulation plays an essential role in stabilizing the flow in the upper layers.

By assuming that the  $\sim 450 \text{ m s}^{-1}$  speed (Hammel *et al.* 1995) of the dark ring seen propagating outward from each of the Comet Shoemaker-Levy 9 impact sites is the gravity wave speed in Jupiter's atmosphere (not a firmly established fact), Dowling (1995b) singled out the corresponding member in the family of deep circulations mentioned above to predict that Jupiter's westward jets change little with depth, but that its eastward jets increase in strength by 50–100% with depth. This prediction for the eastward jets closely matches the subsequent results of the *Galileo* probe Doppler wind experiment, with the caveat that the probe's latitude of  $7^\circ\text{N}$  is too close to the equator for the strong Coriolis effect assumed by this quasigeostrophic (mid-latitude) theory.

### 6.6.3 Banding Controlled in the Interior

Several groups have considered the possibility that Jupiter's jet streams are rooted deep in the interior where the planet's internal heat source drives convection, and where there is no confinement of motions inside a thin spherical shell. Busse (1976) investigated such convection, and showed that it can generate alternating jets at the top of the convecting sphere. Condie and Rhines (1994) studied a laboratory analog consisting of a rotating bowl of warm water that is uniformly cooled at the free surface. The cooling generates convection cells that give rise to azimuthal jets when they encounter the free surface. Manneville and Olson (1996) find symmetric bands and zonal jets in a rotating convecting fluid sphere. Sun *et al.* (1993) carried out numerical simulations of a rapidly rotating, deep fluid shell and achieved a broad eastward flow at the equator with alternating jets at higher latitudes. However, the amplitude of their zonal flow is an order of magnitude less than the amplitude of the non-axisymmetric flow; in other words, the jets are barely discernable through the large noise of the convection. Zhang and Schubert (2000) developed a model that combines convection in the deep interior with an overlying stable atmosphere. They find that strong motions can concentrate in the atmosphere as a result of convection that is driven thermally in the deep interior, a phenomenon they term "teleconvection." More coupled atmosphere-interior models like this one are needed. Eventually the atmospheric component should include effects of moist convection, and the interior component should include the effects of electrical conductivity and magnetic fields.

### 6.6.4 Modes of Internal Heat Transfer

Ingersoll and Porco (1978) pointed out that if Jupiter has a convective interior, only very small lateral temperature gradients should be expected at the outer edge of the convective region. If the emission to space is from the top of the convective interior, it should be uniform with latitude. This is

the accepted explanation for the observation (Figure 6.12) that emission to space on Jupiter is essentially independent of latitude (Ingersoll *et al.* 1976, Pirraglia 1984). But neither the zonal mean insolation nor the emission to space is determined very accurately by observations, and dynamically important temperature gradients at, say, the 10-bar level cannot be ruled out. Temperature contrasts of only a few degrees would be important for the dynamics, and could possibly explain the mean eastward bias in globally averaged surface wind (Gierasch 1999).

A new wrinkle was introduced when Guillot *et al.* (1994) pointed out that a radiative zone might exist in Jupiter (and Saturn) near the depth where the temperature reaches about 2000 K. This occurs where the pressure is a few tens of kilobars and the depth is a few percent of the radius. At this temperature the peak of the Planck function has shifted to near 5  $\mu\text{m}$ , where jovian material has relatively low opacity. Since 1994, Guillot has discovered new sources of opacity, and this radiative zone may not exist on Jupiter. If it does exist, the Ingersoll and Porco reasoning should be reexamined. Gierasch (1999) experimented with radiative-convective models that include a radiative zone and no lateral heat transport. These models show that even a modest radiative zone would break the tight constraint on latitudinal temperature gradients that is imposed by a fully convective interior.

A major question about the outer planets is the depth of the dynamical region that produces the visible jets and spots. Without a solid surface and without a stability transition there is no externally imposed boundary to form a base, leading to debate about “deep cylinder” flow configurations that extend through the planet as opposed to “shallow weather layer” configurations (Busse 1976, Allison 2000). If a radiative zone exists, it could be the location of the “windy jovian thermocline” discussed by Allison (2000). Allison’s thermocline is a stable layer that is conjectured to close off the weather layer circulation and separate it from the deep interior. In general, the basic state stratification is a fundamental parameter affecting dynamics and heat transport and it is of high priority to determine whether a radiative zone exists on Jupiter and Saturn.

### 6.6.5 Banding Controlled by Tides

The third class of hypotheses concerning the control of Jupiter’s jet streams involves the intriguing possibility that the winds are shaped and accelerated by satellite tides. Ioanou and Lindzen (1994) showed that if the interior of Jupiter is even modestly stable to convection, tides that are dominated by higher-order Hough modes can couple to it. These tend to produce banding with alternating accelerations on the order of  $1 \text{ cm s}^{-1} \text{ d}^{-1}$ , which is significant. The authors find that the dominant tides come from Io, Titan, Ariel, and Triton, respectfully, for Jupiter, Saturn, Uranus, and Neptune. This idea adds to the motivation to search for observational evidence of the tidal response at Jupiter’s cloud level.

### 6.6.6 Equatorial Superrotation

Jupiter, Saturn, Venus, and the Sun exhibit equatorial superrotation – the atmosphere rotates faster near the equator

than at other latitudes. Earth, Uranus, and Neptune exhibit equatorial subrotation. Although the equator of Jupiter is a local minimum of zonal velocity due to the zonal jet maxima at  $\pm 7^\circ$  PG latitude (Figure 6.2), it is a local maximum of absolute angular momentum. Since rings of fluid circling the planet at constant latitude tend to conserve their angular momentum as they move, any mixing between rings will reduce the angular momentum at the equator. A theorem due to Hide (1970) states that a circulation that is symmetric about the axis of rotation (one with no eddies) cannot sustain a local maximum of angular momentum. The inference is that the equatorial maximum on Jupiter is maintained by eddy fluxes, e.g., pressure variations in longitude. In a paper on the superrotation of Venus, Gierasch (1975) noted that friction tends to mix angular momentum down the gradient of angular velocity, toward a state of solid body rotation. For Jupiter, this down-gradient mixing is toward the equator, at least up to the latitude of the zonal jets at  $\pm 7^\circ$ . Since friction in a planetary atmosphere involves turbulent eddies, the conclusion is that Jupiter’s equatorial superrotation is maintained by eddy fluxes. Whether the mixing is from higher latitudes or from lower altitudes is unknown.

Most inverse-cascade models (Section 6.6.1) use a  $\beta$ -plane geometry, and so are unable to address the question of equatorial superrotation. Cho and Polvani (1996) consider decaying barotropic turbulence in a thin layer on a full rotating sphere. Zonal jets develop at mid latitudes, but the equator subrotates as on Uranus and Neptune. Yano *et al.* (2002) consider decaying barotropic turbulence in a deep fluid sphere, where the  $\beta$  effect has the opposite sign from that in a shallow surface layer (Ingersoll and Pollard 1982). In this case a superrotating flow develops at the equator as on Jupiter and Saturn. This is a suggestive result, but it is not a proof that the fluid sphere model is correct, since Venus superrotates and Earth does not, and both atmospheres are thin compared to the radius of the planet.

## 6.7 MODELS OF DISCRETE FEATURES

### 6.7.1 Stable Vortices

The simplest model that produces stable vortices is an inviscid, two-dimensional, non-divergent flow with shear (Moore and Saffman 1971, Kida 1981). The fluid has uniform vorticity inside an isolated patch and a different uniform vorticity outside. A steady, stable configuration occurs when the anomalous patch has elliptical shape, with the long axis oriented parallel to the flow at infinity (east–west on the giant planets). The aspect ratio (ratio of long axis to short axis) depends on the ratio of the vorticity inside to that outside the patch. Finite amplitude perturbations lead to stable oscillations in the aspect ratio and orientation.

Polvani *et al.* (1990) showed that this “Kida vortex” model does a good job of matching the observations of vortices on the giant planets. For the GRS and white ovals of Jupiter, where we have measurements of the vorticity inside and outside, the model accurately accounts for the average aspect ratio (Ingersoll *et al.* 1995). For the Great Dark Spot (GDS) of Neptune, which oscillates in aspect ratio and orientation, the model accurately accounts for the relative phase

and relative amplitude of the two oscillations. The model does not explain the amplitude itself, which is a free parameter of the theory, nor does it account for the observed shedding of filaments.

It is remarkable that the Kida vortex model works as well as it does. It has no vertical structure, no gradient in the ambient vorticity ( $\beta$  effect), no forcing, and no dissipation. Introducing these effects adds to the complexity of the models and greatly increases the number of free parameters. In fact, stable vortices exist in models with a wide variety of assumptions about the vertical thermal structure, the flow underneath, and the energy source (Ingersoll and Cuong 1981, Williams and Yamagata 1984, Marcus 1988, Williams and Wilson 1988, Dowling and Ingersoll 1989, Williams 1996, 2002, LeBeau and Dowling 1998, Marcus *et al.* 2000, Cho *et al.* 2001, Youssef and Marcus 2003). Stable vortices form also in laboratory experiments (Nezlin 1986, Read 1986).

The GRS oscillates in longitude with  $\sim 1^\circ$  amplitude (peak-to-peak) and 90-day period (Solberg 1969, Trigo-Rodriguez *et al.* 2000). Other jovian spots oscillate in longitude as well (Peek 1958). Neptune's second dark spot discovered in *Voyager 2* images oscillated in longitude with  $\pm 45^\circ$  amplitude and 36-day period (Ingersoll *et al.* 1995). The Kida model has oscillations in orientation and aspect ratio only. Achterberg and Ingersoll (1994) developed a model in which the longitude oscillations arise when the top and bottom halves of the vortex orbit around a common vertical axis. They obtained peak-to-peak amplitudes up to  $15^\circ$ , but they were not able to reproduce the large-amplitude oscillation of the Neptune spot because the two halves of the vortex tended to separate and drift off separately.

These inviscid theories shed no light on what maintains the vortices or their oscillations against dissipation. Observations of mergers suggest that the large vortices feed on the smaller ones. The inverse cascade of energy from small scales to large scales apparently maintains the vortices as well as the zonal jets. One then must ask where do the small vortices get their energy? The possibilities include: instability associated with latitudinal temperature gradients and the corresponding vertical shear, horizontal shear instability of the zonal jets, and moist convection. Finding the answer is an active area of current research.

### 6.7.2 Statistical Mechanics Models

An entirely different approach, one that bypasses the temporal development of the flow, is to solve for the equilibrium state that maximizes a global integral that is analogous to the entropy in statistical mechanics (Sommeria *et al.* 1991, Miller *et al.* 1992, Michel and Robert 1994, Stegner and Zeitlin 1996, Turkington *et al.* 2001, Bouchet and Sommeria 2002). The parcels are allowed to mix as if they were chemically distinct molecules, such that each parcel conserves its initial value of potential vorticity (PV). This conservative mixing is appropriate for an inviscid, adiabatic fluid, but it is not clear how it would work in a real atmosphere, where the PV values may change during mixing. Also, the initial PV distribution is arbitrary and is not derivable from the maximum-entropy principle. The proponents of this approach point out that the equilibrium states agree with numerical simulation (e.g., Marcus 1988) and with the

steady shapes of jovian vortices. The model does not account for the oscillations, since the equilibrium state is steady.

Turkington *et al.* (2001) propose using the equilibrium statistical theory for inverse modeling of the small-scale vorticity distribution. They start with realistic zonal jets and the underlying zonal flow as defined by Dowling (1995b). The theory gives one GRS, one white oval, and realistic zonal jets – but only if the initial vorticity distribution is skewed toward anticyclonic values. Turkington *et al.* cite the recent *Galileo* results (Gierasch *et al.* 2000, Ingersoll *et al.* 2000) that support the occurrence of intense small-scale anticyclonic forcing.

### 6.7.3 Equatorial Hot Spots and the *Galileo* Probe

In 1995, the *Galileo* probe took in situ measurements of composition, winds, temperature, and clouds from about 0.4 bars to 22 bars, a 150-km range of altitude. These measurements have raised questions about conditions below the clouds. Before the probe's entry, many experts thought that the atmosphere would be well mixed below the condensation levels. That is, the ammonia mixing ratio would level off below 0.7 bars, and the  $\text{H}_2\text{S}$  and water mixing ratios would level off below 2 bars and 6 bars, respectively. Instead the ammonia mixing ratio leveled off at 10 bars,  $\text{H}_2\text{S}$  leveled off at 16 bars, and water was still increasing with depth at 20 bars (Niemann *et al.* 1998, Folkner *et al.* 1998, Mahaffy *et al.* 2000). These observations require a dynamical explanation.

The probe entered one of Jupiter's 5- $\mu\text{m}$  hot spots, where a hole in the visible cloud 5000 km wide allows 5- $\mu\text{m}$  radiation to escape. To explain the hole in the clouds and the depressed volatile abundances, several authors suggested that hot spots contain downdrafts that advect dry air from the upper troposphere down to  $\sim 20$  bars or deeper. The simplest version of this idea has dense air that descends because it is convectively unstable (Atreya *et al.* 1999, Showman and Ingersoll 1998, Baker and Schubert 1998). A difficulty is that any static stability from 1–10 bars (as seems to exist; see Section 6.4.4) would act to halt the descent. Moreover, downdrafts produced in numerical simulations (Baker and Schubert 1998) are two orders of magnitude too small. The convective downdraft hypothesis also has problems with the wind shear, which tends to pull the hot spot apart in 1 or 2 days, and does not explain the layered distribution of volatiles.

The second idea hypothesizes that hot spots are the downwelling branch of an equatorially trapped wave (Friedson and Orton 1999, Showman and Dowling 2000). Allison (1990) and Ortiz *et al.* (1998) documented wavelike behavior for the plumes and hot spots, and Showman and Dowling (2000) performed numerical simulations that support this idea. Air parcels that enter the hot spot from the west (at tens of  $\text{m s}^{-1}$ ) are deflected downward; the parcels return to their original altitudes a few days later as they exit the hot spot to the east. This downwelling wave model explains the layered structure in the ammonia,  $\text{H}_2\text{S}$ , and water. Showman and Dowling's (2000) simulations also suggest that the increase in winds with depth observed by the *Galileo* probe results from local dynamics at the south edge of hot spots and may not be a large-scale property of Jupiter's equatorial atmosphere. Although some issues remain, the model successfully explains the observed dryness as a local me-

teological effect, and it is consistent with the idea that Jupiter's deep water abundance is at least solar.

## 6.8 UNANSWERED QUESTIONS AND POSSIBLE SOLUTIONS

Some of the big questions are: Why are the giant planets banded? What controls the speed and width of the zonal jets? Why are the jets stable? Where do the jets get their energy? Do the winds extend into the fluid interior? Why are the large vortices so stable? What are the clouds made of, and why are they colored? What is the composition of the deep atmosphere? What is the water abundance? How important is moist convection? Where does lightning occur, and what is its relation to global features? Many of these questions concern the deep atmosphere – its composition, thermal structure, and dynamics. Here we describe how observations and modeling can provide the answers.

Gravity measurements can determine whether the deep atmosphere, 1000s of km down, is in solid-body rotation or has jet streams comparable in speed to the surface jets. The centrifugal forces associated with the deep jets cause a re-arrangement of mass that reveals itself in the planet's external gravity field. To sample the higher harmonics of the gravity field, it is best to have a polar orbiter or flyby with a low perijove.

Water is crucial to the meteorology of Jupiter and to the planet's history, since water ice is thought to have played a crucial role in the distribution of volatiles throughout the solar system (see Chapter 2). Both water and ammonia absorb in the microwave region and reveal themselves in the thermal emission coming from the planet at these wavelengths. A microwave radiometer on a spacecraft passing close to the planet could detect this radiation and measure the water and ammonia abundance at depths ranging from 1 bar to 100s of bars.

Probes can measure gaseous abundances, including water, and can also measure temperature, cloud amount, scattered sunlight, and winds. The vertical temperature profile determines the dynamical coupling between the deep atmosphere and the surface layers. Stable stratification means they are uncoupled; neutral or unstable means they are coupled. Sunlight provides energy for the winds, which can be measured by Doppler tracking as the probe descends. A major lesson of the *Galileo* probe mission is that it is important to have multiple probes that enter Jupiter's atmosphere at different latitudes. It is also important that they return data to ~100 bars. Both of these goals are within reach.

Progress will come as well from data already in hand and from theoretical modeling. Most of the *Cassini* data were not analyzed at the time of this writing; they could contain data on chemical tracers, temperatures, winds, water, ammonia, and lightning that answer some fundamental questions. For instance, *Galileo* provided a snapshot of the lightning storms, but *Cassini* may allow us to track the storms over time, measure their motion, and determine their lifetimes. Since the lightning is generated at or below the base of the water cloud, the storms' motion could reveal information about winds at depths that cannot be observed in dayside images.

Numerical models are a key tool for studying atmo-

spheres, and Jupiter's atmosphere is no exception. The data provide constraints on the models. Models of key processes like moist convection in a bottomless atmosphere need to be developed. The GCMs for Jupiter are less well constrained than GCMs for Earth or Mars, but that makes them all the more interesting. Meteorologists and oceanographers recognize Jupiter's value as a fluid dynamics laboratory. The goal is to capture the truth in a small range of parameter space. When the combined constraints of observation and theory rule out most of the hypotheses and the models all resemble each other, then we can truly claim to understand the dynamics of Jupiter's atmosphere.

**Acknowledgements.** We thank the many agencies that have funded planetary science research, and we thank the many people who have contributed to our knowledge of Jupiter's atmosphere.

## REFERENCES

- Achterberg, R. K. and A. P. Ingersoll, A normal-mode approach to jovian atmospheric dynamics, *J. Atmos. Sci.* **46**, 2448–2462, 1989.
- Achterberg, R. K. and A. P. Ingersoll, Numerical simulation of baroclinic jovian vortices, *J. Atmos. Sci.* **51**, 541–562, 1994.
- Allison, M., Planetary waves in Jupiter's equatorial atmosphere, *Icarus* **83**, 282–307, 1990.
- Allison, M., A similarity model for the windy jovian thermocline, *Planet. Space Sci.* **48**, 753–774, 2000.
- Allison, M. and D. H. Atkinson, *Galileo* probe Doppler residuals as the wave-dynamical signature of weakly stable downward-increasing stratification in Jupiter's deep wind layer, *Geophys. Res. Lett.* **28**, 2747–2750, 2001.
- Atkinson, D. H., J. B. Pollack, and A. Seiff, The *Galileo* probe Doppler wind experiment: Measurement of the deep zonal winds on Jupiter, *J. Geophys. Res.* **103**, 22911–22928, 1998.
- Atreya, S. K., *Atmospheres and Ionospheres of the Outer Planets and their Satellites*, Springer-Verlag, 1986.
- Atreya, S. K., M. H. Wong, T. C. Owen, P. R. Mahaffy, H. B. Niemann, I. de Pater, P. Drossart, and T. Encrenaz, A comparison of the atmospheres of Jupiter and Saturn: Deep atmospheric composition, cloud structure, vertical mixing, and origin, *Planet. Space Sci.* **47**, 1243–1262, 1999.
- Baker, R. D. and G. Schubert, Deep convective entrainment by downdrafts in Jupiter's atmosphere, *Icarus* **136**, 340–343, 1998.
- Banfield, D., P. J. Gierasch, M. Bell, E. Ustinov, A. P. Ingersoll, A. R. Vasavada, R. A. West, and M. J. S. Belton, Jupiter's cloud structure from *Galileo* imaging data, *Icarus* **135**, 230–250, 1998.
- Barcilon, A. and P. J. Gierasch, A moist, Hadley cell model for Jupiter's cloud bands, *J. Atmos. Sci.* **27**, 550–560, 1970.
- Beebe, R. F. and T. A. Hockey, A comparison of red spots in the atmosphere of Jupiter, *Icarus* **67**, 96–105, 1986.
- Beebe, R. F. and L. A. Youngblood, Pre-*Voyager* velocities, accelerations and shrinkage rates of jovian cloud features, *Nature* **280**, 771–772, 1979.
- Beebe, R. F., A. P. Ingersoll, G. E. Hunt, J. L. Mitchell, and J.-P. Muller, Measurements of wind vectors, eddy momentum transports, and energy conversions in Jupiter's atmosphere from *Voyager 1* images, *Geophys. Res. Lett.* **7**, 1–4, 1980.
- Beebe, R. F., G. S. Orton, and R. A. West, Time-variable nature of the Jovian cloud properties and thermal structure: An observational perspective, in *Time-Variable Phenomena in*

- the Jovian System, M.J.S. Belton, R.A. West, J. Rahe (eds), NASA, pp. 245–288, 1989.
- Beebe, R. F., A. A. Simon, and L. F. Huber, Comparison of *Galileo* probe and Earth-based translation rates of Jupiter's equatorial clouds, *Science* **272**, 841, 1996.
- Borucki, W. J. and J. A. Magalhaes, Analysis of *Voyager 2* images of jovian lightning, *Icarus* **96**, 1–14, 1992.
- Borucki, W. J. and M. A. Williams, Lightning in the jovian water cloud, *J. Geophys. Res.* **91**, 9893–9903, 1986.
- Borucki, W. J., A. Bar-Nun, F. L. Scarf, A. F. Cook, and G. E. Hunt, Lightning activity on Jupiter, *Icarus* **52**, 492–502, 1982.
- Borucki, W. J., C. P. McKay, D. Jebens, H. S. Lakkara, and C. T. Vanajakshi, Spectral irradiance measurements of simulated lightning in planetary atmospheres, *Icarus* **123**, 336–344, 1996.
- Bosak, T. and A. P. Ingersoll, Shear instabilities as a probe of Jupiter's atmosphere, *Icarus* **158**, 401–409, 2002.
- Bouchet, F. and J. Sommeria, Emergence of intense jets and Jupiter's Great Red Spot as maximum-entropy structures, *J. Fluid Mech.* **464**, 165–207, 2002.
- Busse, F. H., A simple model of convection in the jovian atmosphere, *Icarus* **29**, 255–260, 1976.
- Cho, J. Y.-K. and L. M. Polvani, The morphogenesis of bands and zonal winds in the atmospheres on the giant outer planets, *Science* **273**, 335–337, 1996.
- Cho, J. Y.-K., M. de La Torre Juárez, A. P. Ingersoll, and D. G. Dritschel, A high-resolution, three-dimensional model of Jupiter's Great Red Spot, *J. Geophys. Res.* **106**, 5099–5105, 2001.
- Condie, S. A. and P. B. Rhines, Topographic Hadley cells, *J. Fluid Mech.* **280**, 349–368, 1994.
- Conrath, B. J. and P. J. Gierasch, Global variation of the para hydrogen fraction in Jupiter's atmosphere and implications for dynamics on the outer planets, *Icarus* **57**, 184–204, 1984.
- Conrath, B. J. and P. J. Gierasch, Retrieval of ammonia abundances and cloud opacities on Jupiter from *Voyager* IRIS spectra, *Icarus* **67**, 444–455, 1986.
- Conrath, B. J., F. M. Flasar, J. A. Pirraglia, P. J. Gierasch, and G. E. Hunt, Thermal structure and dynamics of the jovian atmosphere: 2. Visible cloud features, *J. Geophys. Res.* **86**, 8769–8775, 1981.
- Conrath, B. J., P. J. Gierasch, and S. S. Leroy, Temperature and circulation in the stratosphere of the outer planets, *Icarus* **83**, 255–281, 1990.
- Delgenio, A. D. and K. B. McGrattan, Moist convection and the vertical structure and water abundance of Jupiter's atmosphere, *Icarus* **84**, 29–53, 1990.
- Deming, D., M. J. Mumma, F. Espenak, D. E. Jennings, T. Kostiuik, G. Wiedemann, R. Loewenstein, and J. Piscitelli, A search for P-mode oscillations of Jupiter: Serendipitous observations of nonacoustic thermal wave structure, *ApJ* **343**, 456–467, 1989.
- Deming, D., D. Reuter, D. Jennings, G. Bjoraker, G. McCabe, K. Fast, and G. Wiedemann, Observations and analysis of longitudinal thermal waves on Jupiter, *Icarus* **126**, 301–312, 1997.
- Dowling, T. E., A relationship between potential vorticity and zonal wind on Jupiter, *J. Atmos. Sci.* **50**, 14–22, 1993.
- Dowling, T. E., Dynamics of jovian atmospheres, *Annual Review of Fluid Mechanics* **27**, 293–334, 1995a.
- Dowling, T. E., Estimate of Jupiter's deep zonal-wind profile from Shoemaker–Levy 9 data and Arnol'd's second stability criterion, *Icarus* **117**, 439–442, 1995b.
- Dowling, T. E. and A. P. Ingersoll, Potential vorticity and layer thickness variations in the flow around Jupiter's Great Red Spot and white oval BC, *J. Atmos. Sci.* **45**, 1380–1396, 1988.
- Dowling, T. E. and A. P. Ingersoll, Jupiter's Great Red spot as a shallow water system, *J. Atmos. Sci.* **46**, 3256–3278, 1989.
- Dyudina, U. A., A. P. Ingersoll, A. R. Vasavada, S. P. Ewald, and the *Galileo* SSI Team, Monte Carlo radiative transfer modeling of lightning observed in *Galileo* images of Jupiter, *Icarus* **160**, 336–349, 2002.
- Fisher, B. M., *High Time Resolution Infrared Imaging Observations of Jupiter*, Ph.D. thesis, University of California, San Diego, 1994.
- Fisher, B. M., G. S. Orton, and C. Hasenkopf, Jovian longitudinal thermal structure in mid 1999, *BAAS* **33**, 1045, 2001.
- Flasar, F. M., Temporal behavior of Jupiter's meteorology, in *Time-Variable Phenomena in the Jovian System*, M. J. S. Belton, R. A. West, J. Rahe (eds), NASA, pp. 324–343, 1989.
- Flasar, F. M. and P. J. Gierasch, Mesoscale waves as a probe of Jupiter's deep atmosphere, *J. Atmos. Sci.* **43**, 2683–2707, 1986.
- Flasar, F. M., B. J. Conrath, J. Pirraglia, P. C. Clark, R. G. French, and P. J. Gierasch, Thermal structure and dynamics of the jovian atmosphere: 1. The Great Red Spot, *J. Geophys. Res.* **86**, 8759–8767, 1981.
- Folkner, W. M., R. Woo, and S. Nandi, Ammonia abundance in Jupiter's atmosphere derived from the attenuation of the *Galileo* probe's radio signal, *J. Geophys. Res.* **103**, 22 847–22 855, 1998.
- Friedson, A. J., New observations and modelling of a QBO-like oscillation in Jupiter's stratosphere, *Icarus* **137**, 34–55, 1999.
- Friedson, A. J. and G. S. Orton, A dynamical model of Jupiter's 5-micron hot spots, *BAAS* **31**, 1155, 1999.
- García-Melendo, E. and A. Sánchez-Lavega, A study of the stability of jovian zonal winds from HST images: 1995–2000, *Icarus* **152**, 316–330, 2001.
- García-Melendo, E., A. Sánchez-Lavega, J. M. Gómez, J. Lecacheux, F. Colas, I. Miyazaki, and D. Parker, Long-lived vortices and profile changes in the 23.7°N high-speed jovian jet, *Icarus* **146**, 514–524, 2000.
- Gehrels, T., *Jupiter*, University of Arizona Press, 1976.
- Gierasch, P. J., Meridional circulation and the maintenance of the Venus atmospheric rotation, *J. Atmos. Sci.* **32**, 1038–1044, 1975.
- Gierasch, P. J., Radiative-convective latitudinal gradients for Jupiter and Saturn models with a radiative zone, *Icarus* **142**, 148–154, 1999.
- Gierasch, P. J. and B. J. Conrath, Dynamics of the atmospheres of the outer planets: Post-*Voyager* measurement objectives, *J. Geophys. Res.* **98**, 5459–5469, 1993.
- Gierasch, P. J., B. J. Conrath, and J. A. Magalhaes, Zonal mean properties of Jupiter's upper troposphere from *Voyager* infrared observations, *Icarus* **67**, 456–483, 1986.
- Gierasch, P. J., A. P. Ingersoll, D. Banfield, S. P. Ewald, P. Helfenstein, A. Simon-Miller, A. Vasavada, H. H. Breneman, D. A. Senske, and the *Galileo* Imaging Team, Observation of moist convection in Jupiter's atmosphere, *Nature* **403**, 628–630, 2000.
- Guillot, T., G. Chabrier, P. Morel, and D. Gautier, Nonadiabatic models of Jupiter and Saturn, *Icarus* **112**, 354–367, 1994.
- Hammel, H. B., R. F. Beebe, A. P. Ingersoll, G. S. Orton, J. R. Mills, A. A. Simon, P. Chodas, J. T. Clarke, E. De Jong, T. E. Dowling, J. Harrington, L. F. Huber, E. Karkoschka, C. M. Santori, A. Toigo, D. Yeomans, and R. A. West, HST imaging of atmospheric phenomena created by the impact of Comet Shoemaker–Levy 9, *Science* **267**, 1288–1296, 1995.
- Harrington, J., T. E. Dowling, and R. L. Baron, Jupiter's tropospheric thermal emission: 2. Power spectrum analysis and wave search, *Icarus* **124**, 32–44, 1996.
- Hatzes, A., D. D. Wenkert, A. P. Ingersoll, and G. E. Danielson, Oscillations and velocity structure of a long-lived cyclonic spot, *J. Geophys. Res.* **86**, 8745–8749, 1981.
- Hess, S. L. and H. A. Panofsky, The atmospheres of the other

- planets, in *Compendium of Meteorology*, T. F. Malone (ed.), American Meteorological Society, pp. 391–400, 1951.
- Hide, R., Equatorial jets in planetary atmospheres, *Nature* **225**, 254, 1970.
- Huang, H. P. and W. A. Robinson, Two-dimensional turbulence and persistent zonal jets in a global barotropic model, *J. Atmos. Sci.* **55**, 611–632, 1998.
- Hueso, R. and A. Sánchez-Lavega, A three-dimensional model of moist convection for the giant planets: The Jupiter case, *Icarus* **151**, 257–274, 2001.
- Hueso, R., A. Sánchez-Lavega, and T. Guillot, A model for large-scale convective storms in Jupiter, *J. Geophys. Res.* **107**, E10, 2002.
- Hunt, G. E., B. J. Conrath, and J. Pirraglia, Visible and infrared observations of jovian plumes during the *Voyager* encounter, *J. Geophys. Res.* **86**, 8777–8781, 1981.
- Ingersoll, A. P., *Pioneer 10* and *11* observations and the dynamics of Jupiter's atmosphere, *Icarus* **29**, 245–253, 1976a.
- Ingersoll, A. P., The atmosphere of Jupiter, *Space Sci. Rev.* **18**, 603–639, 1976b.
- Ingersoll, A. P., Atmospheric dynamics of the outer planets, *Science* **248**, 308–315, 1990.
- Ingersoll, A. P. and P. G. Cuong, Numerical model of long-lived jovian vortices, *J. Atmos. Sci.* **38**, 2067–2076, 1981.
- Ingersoll, A. P. and J. N. Cuzzi, Dynamics of Jupiter's cloud bands, *J. Atmos. Sci.* **26**, 981–985, 1969.
- Ingersoll, A. P. and H. Kanamori, Waves from the collisions of Comet Shoemaker–Levy 9 with Jupiter, *Nature* **374**, 706–708, 1995.
- Ingersoll, A. P. and D. Pollard, Motion in the interiors and atmospheres of Jupiter and Saturn: Scale analysis, anelastic equations, barotropic stability criterion, *Icarus* **52**, 62–80, 1982.
- Ingersoll, A. P. and C. C. Porco, Solar heating and internal heat flow on Jupiter, *Icarus* **35**, 27–43, 1978.
- Ingersoll, A. P., G. Munch, G. Neugebauer, and G. S. Orton, Results of the infrared radiometer experiment on *Pioneers 10* and *11*, in *Jupiter*, T. Gehrels (ed), U. of Arizona Press, pp. 197–205, 1976.
- Ingersoll, A. P., R. F. Beebe, J. L. Mitchell, G. W. Garneau, G. M. Yagi, and J.-P. Muller, Interaction of eddies and mean zonal flow on Jupiter as inferred from *Voyager 1* and *2* images, *J. Geophys. Res.* **86**, 8733–8743, 1981.
- Ingersoll, A. P., C. D. Barnet, R. F. Beebe, F. M. Flasar, D. P. Hinson, S. S. Limaye, L. A. Sromovsky, and V. E. Suomi, Dynamic meteorology of Neptune, in *Neptune and Triton*, D. P. Cruikshank (ed), U. of Arizona Press, pp. 613–682, 1995.
- Ingersoll, A. P., P. J. Gierasch, D. Banfield, A. R. Vasavada, and the *Galileo* Imaging Team, Moist convection as an energy source for the large-scale motions in Jupiter's atmosphere, *Nature* **403**, 630–632, 2000.
- Ioannou, P. J. and R. S. Lindzen, Gravitational tides on Jupiter: 3. Atmospheric response and mean flow acceleration, *ApJ* **424**, 1005–1013, 1994.
- Kida, S., Motion of an elliptic vortex in a uniform shear flow, *Phys. Soc. Japan* **50**, 3517–3520, 1981.
- Kirk, R. L. and D. J. Stevenson, Hydromagnetic constraints on deep zonal flow in the giant planets, *ApJ* **316**, 836–846, 1987.
- Lebeau, R. P. and T. E. Dowling, EPIC simulations of time-dependent, three-dimensional vortices with application to Neptune's Great Dark Spot, *Icarus* **132**, 239–265, 1998.
- Leovy, C. B., A. J. Friedson, and G. S. Orton, The quasi-quadrennial oscillation of Jupiter's equatorial stratosphere, *Nature* **354**, 380–382, 1991.
- Li, X. and P. L. Read, A mechanistic model of the quasi-quadrennial oscillation in Jupiter's stratosphere, *Planet. Space Sci.* **48**, 637–669, 2000.
- Limaye, S. S., Jupiter: New estimates of the mean zonal flow at the cloud level, *Icarus* **65**, 335–352, 1986.
- Lindal, G. F., G. E. Wood, G. S. Levy, J. D. Anderson, D. N. Sweetnam, H. B. Hotz, B. J. Buckles, D. P. Holmes, P. E. Doms, V. R. Eshleman, G. L. Tyler, and T. A. Croft, The atmosphere of Jupiter: An analysis of the *Voyager* radio occultation measurements, *J. Geophys. Res.* **86**, 8721–8727, 1981.
- Little, B., C. D. Anger, A. P. Ingersoll, A. R. Vasavada, D. A. Senske, H. H. Breneman, W. J. Borucki, and the *Galileo* SSI Team, *Galileo* images of lightning on Jupiter, *Icarus* **142**, 306–323, 1999.
- Lunine, J. I. and D. M. Hunten, Moist convection and the abundance of water in the troposphere of Jupiter, *Icarus* **69**, 566–570, 1987.
- Mac Low, M.-M. and A. P. Ingersoll, Merging of vortices in the atmosphere of Jupiter: An analysis of *Voyager* images, *Icarus* **65**, 353–369, 1986.
- Magalhães, J. A., A. L. Weir, B. J. Conrath, P. J. Gierasch, and S. S. Leroy, Slowly moving thermal features on Jupiter, *Nature* **337**, 444–447, 1989.
- Magalhães, J. A., A. Seiff, and R. E. Young, The stratification of Jupiter's troposphere at the *Galileo* probe entry site, *Icarus* **158**, 410–433, 2002.
- Mahaffy, P. R., H. B. Niemann, A. Alpert, S. K. Atreya, J. Demick, T. M. Donahue, D. N. Harpold, and T. C. Owen, Noble gas abundance and isotope ratios in the atmosphere of Jupiter from the *Galileo* Probe Mass Spectrometer, *J. Geophys. Res.* **105**, 15 061–15 071, 2000.
- Manneville, J. and P. Olson, Banded convection in rotating fluid spheres and the circulation of the jovian atmosphere, *Icarus* **122**, 242–250, 1996.
- Marcus, P. S., Numerical simulation of Jupiter's Great Red Spot, *Nature* **331**, 693–696, 1988.
- Marcus, P. S., Jupiter's Great Red Spot and other vortices, *ARA&A* **31**, 523–573, 1993.
- Marcus, P. S. and C. Lee, A model for eastward and westward jets in laboratory experiments and planetary atmospheres, *Phys. Fluids* **10**, 1474–1489, 1998.
- Marcus, P. S., T. Kundu, and C. Lee, Vortex dynamics and zonal flows, *Phys. Plasmas* **7**, 1630–1640, 2000.
- Michel, J. and R. Robert, Statistical mechanical theory of the Great Red Spot of Jupiter, *J. Stat. Phys.* **77**, 645–666, 1994.
- Miller, J., P. B. Weichman, and M. C. Cross, Statistical mechanics, Euler's equation, and Jupiter's Red Spot, *Phys. Rev. A* **45**, 2328–2359, 1992.
- Mitchell, J. L., R. J. Terrile, B. A. Smith, J.-P. Muller, A. P. Ingersoll, G. E. Hunt, S. A. Collins, and R. F. Beebe, Jovian cloud structure and velocity fields, *Nature* **280**, 776–778, 1979.
- Mitchell, J. L., R. F. Beebe, A. P. Ingersoll, and G. W. Garneau, Flow fields within Jupiter's Great Red Spot and white oval BC, *J. Geophys. Res.* **86**, 8751–8757, 1981.
- Moore, D. W. and P. G. Saffman, Structure of a line vortex in an imposed strain, in *Aircraft Wake Turbulence and its Detection*, J. H. Olson, A. Goldberg, M. Rogers (eds), Plenum Press, pp. 339–354, 1971.
- Morales-Juberías, R., A. Sánchez-Lavega, J. Lecacheux, and F. Colas, A comparative study of jovian anticyclone properties from a six-year (1994–2000) survey, *Icarus* **157**, 76–90, 2002a.
- Morales-Juberías, R., A. Sánchez-Lavega, J. Lecacheux, and F. Colas, A comparative study of jovian cyclonic features from a six-year (1994–2000) survey, *Icarus* **160**, 325–335, 2002b.
- Moreno, F. and J. Sedano, Radiative balance and dynamics in the stratosphere of Jupiter: Results from a latitude-dependent aerosol heating model, *Icarus* **130**, 36–48, 1997.
- Nakajima, K., S. Takehiro, M. Ishiwatari, and Y. Hayashi, Numerical modeling of Jupiter's moist convection layer, *Geophys. Res. Lett.* **27**, 3129–3132, 2000.

- Nezlin, M. V., Rossby solitons (experimental studies and a laboratory model of natural vortices of the jovian Great Red Spot type), *Uspekhi Fiz. Nauk* **150**, 3–60, 1986.
- Niemann, H. B., S. K. Atreya, G. R. Carignan, T. M. Donahue, J. A. Haberman, D. N. Harpold, R. E. Hartle, D. M. Hunten, W. T. Kasprzak, P. R. Mahaffy, T. C. Owen, and S. H. Way, The composition of the jovian atmosphere as determined by the *Galileo* Probe Mass Spectrometer, *J. Geophys. Res.* **103**, 22 831–22 845, 1998.
- Orsolini, Y. and C. B. Leovy, A model of large-scale instabilities in the jovian troposphere: 1. Linear model, *Icarus* **106**, 392–405, 1993a.
- Orsolini, Y. and C. B. Leovy, A model of large-scale instabilities in the jovian troposphere: 2. Quasi-linear model, *Icarus* **106**, 406–418, 1993b.
- Ortiz, J. L., G. S. Orton, A. J. Friedson, S. T. Stewart, B. M. Fisher, and J. R. Spencer, Evolution and persistence of 5-micron hot spots at the *Galileo* probe entry latitude, *J. Geophys. Res.* **103**, 23 051–23 069, 1998.
- Orton, G. S., A. J. Friedson, J. Caldwell, H. B. Hammel, K. H. Baines, J. T. Bergstralh, T. Z. Martin, M. E. Malcom, R. A. West, W. F. Golisch, D. M. Griep, C. D. Kaminski, A. T. Tokunaga, R. Baron, and M. Shure, Thermal maps of Jupiter: Spatial organization and time dependence of stratospheric temperatures, 1980 to 1990, *Science* **252**, 537–542, 1991.
- Orton, G. S., A. J. Friedson, P. A. Yanamandra-Fisher, J. Caldwell, H. B. Hammel, K. H. Baines, J. T. Bergstralh, T. Z. Martin, R. A. West, G. J. Veeder, D. K. Lynch, R. Russell, M. E. Malcom, W. F. Golisch, D. M. Griep, C. D. Kaminski, A. T. Tokunaga, T. Herbst, and M. Shure, Spatial organization and time dependence of Jupiter's tropospheric temperatures, 1980–1993, *Science* **265**, 625–631, 1994.
- Orton, G. S., J. R. Spencer, L. D. Travis, T. Z. Martin, and L. K. Tamppari, *Galileo* photopolarimeter-radiometer observations of Jupiter and the Galilean satellites, *Science* **274**, 389–391, 1996.
- Orton, G. S., B. M. Fisher, K. H. Baines, S. T. Stewart, A. J. Friedson, J. L. Ortiz, M. Marinova, M. Ressler, A. Dayal, W. Hoffmann, J. Hora, S. Hinkley, V. Krishnan, M. Masanovic, J. Tesic, A. Tsiolas, and K. C. Parija, Characteristics of the *Galileo* probe entry site from Earth-based remote sensing observations, *J. Geophys. Res.* **103**, 22 791–22 814, 1998.
- Panetta, R. L., Zonal jets in wide baroclinically unstable regions: Persistence and scale selection, *J. Atmos. Sci.* **50**, 2073–2106, 1993.
- Pedlosky, J., *Geophysical Fluid Dynamics*, Second Edition, Springer-Verlag, 1987.
- Peek, B. M., *The Planet Jupiter*, Faber & Faber, 1958.
- Pirraglia, J. A., Meridional energy balance of Jupiter, *Icarus* **59**, 169–176, 1984.
- Pirraglia, J. A., Dissipationless decay of jovian jets, *Icarus* **79**, 196–207, 1989.
- Poincaré, H., Sur la precession des corps deformables, *Bull. Astron.* **20**, 321–356, 1910.
- Polvani, L. M., J. Wisdom, E. De Jong, and A. P. Ingersoll, Simple dynamical models of Neptune's Great Dark Spot, *Science* **249**, 1393–1398, 1990.
- Porco, C., R. A. West, A. McEwen, A. D. Del Genio, A. P. Ingersoll, P. Thomas, S. Squyres, L. Dones, C. D. Murray, T. V. Johnson, J. A. Burns, A. Brahic, G. Neukum, J. Veverka, J. M. Barbara, T. Denk, M. Evans, J. J. Ferrier, P. Geissler, P. Helfenstein, T. Roatsch, H. Throop, M. Tiscareno, and A. R. Vasavada, *Cassini* imaging science of Jupiter's atmosphere, satellites, and rings, *Science* **299**, 1541–1547, 2003.
- Rages, K., R. Beebe, and D. Senske, Jovian stratospheric hazes: The high phase angle view from *Galileo*, *Icarus* **139**, 211–226, 1999.
- Read, P. L., Stable, baroclinic eddies on Jupiter and Saturn: A laboratory analog and some observational tests, *Icarus* **65**, 304–334, 1986.
- Rhines, P. B., Waves and turbulence on a beta-plane, *J. Fluid Mech.* **69**, 417–443, 1975.
- Rinnert, K., L. J. Lanzerotti, M. A. Uman, G. Dehmel, F. O. Gliem, E. P. Krider, and J. Bach, Measurements of radio frequency signals from lightning in Jupiter's atmosphere, *J. Geophys. Res.* **103**, 22 979–22 992, 1998.
- Rogers, J. H., *The Giant Planet Jupiter*, Cambridge University Press, 1995.
- Roos-Serote, M., A. R. Vasavada, L. Kamp, P. Drossart, P. Irwin, C. Nixon, and R. W. Carlson, Proximate humid and dry regions in Jupiter's atmosphere indicate complex local meteorology, *Nature* **405**, 158–160, 2000.
- Sada, P. V., R. F. Beebe, and B. J. Conrath, Comparison of the structure and dynamics of Jupiter's Great Red Spot between the *Voyager 1* and *2* encounters, *Icarus* **119**, 311–335, 1996.
- Sánchez-Lavega, A. and J. M. Gomez, The South Equatorial Belt of Jupiter: 1. Its life cycle, *Icarus* **121**, 1–17, 1996.
- Sánchez-Lavega, A. and R. Rodrigo, Ground based observations of synoptic cloud systems in southern equatorial to temperate latitudes of Jupiter from 1975 to 1983, *A&A* **148**, 67–78, 1985.
- Sánchez-Lavega, A., I. Miyazaki, D. Parker, P. Laques, and J. Lecacheux, A disturbance in Jupiter's high-speed north temperate jet during 1990, *Icarus* **94**, 92–97, 1991.
- Sánchez-Lavega, A., R. Hueso, and J. R. Acarreta, A system of circumpolar waves in Jupiter's stratosphere, *Geophys. Res. Lett.* **25**, 4043–4046, 1998a.
- Sánchez-Lavega, A., R. Hueso, J. Lecacheux, F. Colas, J. F. Rojas, J. M. Gomez, I. Miyazaki, and D. Parker, Dynamics and interaction between a large-scale vortex and the Great Red Spot in Jupiter, *Icarus* **136**, 14–26, 1998b.
- Sánchez-Lavega, A., J. F. Rojas, R. Hueso, J. Lecacheux, F. Colas, J. R. Acarreta, I. Miyazaki, and D. Parker, Interaction of jovian white ovals BC and DE in 1998 from Earth-based observations in the visual range, *Icarus* **142**, 116–124, 1999.
- Sánchez-Lavega, A., G. S. Orton, R. Morales, J. Lecacheux, F. Colas, B. Fisher, P. Fukumura-Sawada, W. Golisch, D. Griep, C. Kaminski, K. Baines, K. Rages, and R. West, The merger of two giant anticyclones in the atmosphere of Jupiter, *Icarus* **149**, 491–495, 2001.
- Seiff, A., D. B. Kirk, T. C. D. Knight, R. E. Young, J. D. Mihalov, L. A. Young, F. S. Milos, G. Schubert, R. C. Blanchard, and D. Atkinson, Thermal structure of Jupiter's atmosphere near the edge of a 5-micron hot spot in the North Equatorial Belt, *J. Geophys. Res.* **103**, 22 857–22 889, 1998.
- Showman, A. P. and T. E. Dowling, Nonlinear simulations of Jupiter's 5-micron hot spots, *Science* **289**, 1737–1740, 2000.
- Showman, A. P. and A. P. Ingersoll, Interpretation of *Galileo* probe data and implications for Jupiter's dry downdrafts, *Icarus* **132**, 205–220, 1998.
- Simon, A. A., R. F. Beebe, P. J. Gierasch, A. R. Vasavada, and M. J. S. Belton, Global context of the *Galileo* E6 observations of Jupiter's white ovals, *Icarus* **135**, 220–229, 1998.
- Simon-Miller, A. A., D. Banfield, and P. J. Gierasch, An HST study of jovian chromophores, *Icarus* **149**, 94–106, 2001a.
- Simon-Miller, A. A., D. Banfield, and P. J. Gierasch, Color and the vertical structure in Jupiter's belts, zones, and weather systems, *Icarus* **154**, 459–474, 2001b.
- Simon-Miller, A. A., P. J. Gierasch, R. F. Beebe, B. Conrath, F. M. Flasar, R. K. Achterberg, and the *Cassini* CIRS Team, New observational results concerning Jupiter's Great Red Spot, *Icarus* **158**, 249–266, 2002.
- Smith, B. A. and G. E. Hunt, Motions and morphology of clouds in the atmosphere of Jupiter, in *Jupiter*, T. Gehrels (ed), University of Arizona Press, pp. 564–585, 1976.

- Smith, B. A., L. A. Soderblom, T. V. Johnson, A. P. Ingersoll, S. A. Collins, E. M. Shoemaker, G. E. Hunt, H. Masursky, M. H. Carr, M. E. Davies, A. F. Cook II, J. M. Boyce, G. E. Danielson, T. Owen, C. Sagan, R. F. Beebe, J. Veverka, R. G. Strom, J. F. McCauley, D. Morrison, G. A. Briggs, and V. E. Suomi, The Jupiter system through the eyes of *Voyager 1*, *Science* **204**, 951–972, 1979a.
- Smith, B. A., L. A. Soderblom, R. Beebe, J. Boyce, G. Briggs, M. Carr, S. A. Collins, A. F. Cook II, G. E. Danielson, M. E. Davies, G. E. Hunt, A. P. Ingersoll, T. V. Johnson, H. Masursky, J. F. McCauley, D. Morrison, T. Owen, C. Sagan, E. M. Shoemaker, R. G. Strom, V. E. Suomi, and J. Veverka, The Galilean satellites and Jupiter: *Voyager 2* imaging science results, *Science* **206**, 927–950, 1979b.
- Smith, M. D. and P. J. Gierasch, Convection in the outer planet atmospheres including ortho-para hydrogen conversion, *Icarus* **116**, 159–179, 1995.
- Solberg, Jr., H. G., A 3-month oscillation in the longitude of Jupiter's Red Spot, *Space Sci. Rev.* **17**, 1573–1580, 1969.
- Sommeria, J., C. Nore, T. Dumont, and R. Robert, Statistical theory of the Great Red Spot of Jupiter, *Comptes Rendus de L'Academie des Sciences Paris Serie II* **312**, 999–1005, 1991.
- Sromovsky, L. A., H. E. Revercomb, V. E. Suomi, S. S. Limaye, and R. J. Kraus, Jovian winds from *Voyager 2*: 2. Analysis of eddy transports, *J. Atmos. Sci.* **39**, 1433–1445, 1982.
- Stegner, A. and V. Zeitlin, Asymptotic expansions and monopolar solitary Rossby vortices in barotropic and two-layer models, *Geophys. Astrophys. Fluid Dyn.* **83**, 159–194, 1996.
- Stoker, C. R., Moist convection: A mechanism for producing the vertical structure of the jovian equatorial plumes, *Icarus* **67**, 106–125, 1986.
- Stone, P. H., The meteorology of the jovian atmosphere, in *Jupiter*, T. Gehrels (ed), University of Arizona Press, pp. 586–618, 1976.
- Sukoriansky, S., B. Galperin, and N. Dikovskaya, Universal spectrum of two-dimensional turbulence on a rotating sphere and some basic features of atmospheric circulation on giant planets, *Phys. Rev. Lett.* **89**, 124 501, 2002.
- Sun, Z.-P., G. Schubert, and G. A. Glatzmaier, Banded surface flow maintained by convection in a model of the rapidly rotating giant planets, *Science* **260**, 661–664, 1993.
- Terrile, R. J. and R. F. Beebe, Summary of historical data: Interpretation of the *Pioneer* and *Voyager* cloud configurations in a time-dependent framework, *Science* **204**, 948–951, 1979.
- Terrile, R. J. and J. A. Westphal, The vertical cloud structure of Jupiter from 5 micron measurements, *Icarus* **30**, 274–281, 1977.
- Trigo-Rodriguez, J. M., A. Sánchez-Lavega, J. M. Gómez, J. Lecacheux, F. Colas, and I. Miyazaki, The 90-day oscillations of Jupiter's Great Red Spot revisited, *Planet. Space Sci.* **48**, 331–339, 2000.
- Turkington, B., A. Majda, K. Haven, and M. DiBattista, Statistical equilibrium predictions of jets and spots on Jupiter, *Proc. Natl. Acad. Sci. USA* **98**, 12 346–12 350, 2001.
- Vallis, G. K. and M. E. Maltrud, Generation of mean flows and jets on a beta-plane and over topography, *J. Phys. Oceanogr.* **23**, 1346–1362, 1993.
- Vasavada, A. R., A. P. Ingersoll, D. Banfield, M. Bell, P. J. Gierasch, M. J. S. Belton, G. S. Orton, K. P. Klaasen, E. De Jong, H. H. Breneman, T. J. Jones, J. M. Kaufman, K. P. Magee, and D. A. Senske, *Galileo* imaging of Jupiter's atmosphere: The Great Red Spot, equatorial region, and white ovals, *Icarus* **135**, 265–275, 1998.
- Vincent, M. B., J. T. Clarke, G. E. Ballester, W. M. Harris, R. A. West, J. T. Trauger, R. W. Evans, K. R. Stapelfeldt, D. Crisp, C. J. Burrows, J. S. Gallagher, R. E. Griffiths, J. Jeff Hester, J. G. Hoessel, J. A. Holtzman, J. R. Mould, P. A. Scowen, A. M. Watson, and J. A. Westphal, Jupiter's polar regions in the ultraviolet as imaged by HST/WFPC2: Auroral-aligned features and zonal motions, *Icarus* **143**, 205–222, 2000.
- Walterscheid, R. L., D. G. Brinkman, and G. Schubert, Wave disturbances from the Comet SL9 impacts into Jupiter's atmosphere, *Icarus* **145**, 140–146, 2000.
- West, R. A., A. J. Friedson, and J. F. Appleby, Jovian large-scale stratospheric circulation, *Icarus* **100**, 245–259, 1992.
- Williams, G. P., Planetary circulations: 1. Barotropic representation of jovian and terrestrial turbulence, *J. Atmos. Sci.* **35**, 1399–1426, 1978.
- Williams, G. P., Jovian and comparative atmospheric modeling, *Adv. Geophys.* **28**, 381–429, 1985.
- Williams, G. P., Jovian dynamics: 1. Vortex stability, structure, and genesis, *J. Atmos. Sci.* **53**, 2685–2734, 1996.
- Williams, G. P., Jovian dynamics: Part II. The genesis and equilibration of vortex sets, *J. Atmos. Sci.* **59**, 1356–1370, 2002.
- Williams, G. P. and R. J. Wilson, The stability and genesis of Rossby vortices, *J. Atmos. Sci.* **45**, 207–241, 1988.
- Williams, G. P. and T. Yamagata, Geostrophic regimes, intermediate solitary vortices and jovian eddies, *J. Atmos. Sci.* **41**, 453–478, 1984.
- Yair, Y., Z. Levin, and S. Tzivion, Lightning generation in a jovian thundercloud: Results from an axisymmetric numerical cloud model, *Icarus* **115**, 421–434, 1995.
- Yair, Y., Z. Levin, and S. Tzivion, Model interpretation of jovian lightning activity and the *Galileo* probe results, *J. Geophys. Res.* **103**, 14 157–14 166, 1998.
- Yano, J., O. Talagrand, and P. Drossart, Atmospheric zonal jets in the atmospheres of the giant planets simulated by an idealized two-dimensional deep-fluid model, *Nature* **421**, 36–38, 2003.
- Youssef, A. and P. S. Marcus, The dynamics of jovian white ovals from formation to merger, *Icarus* **162**, 74–93, 2003.
- Zhang, K. and G. Schubert, Teleconvection: Remotely driven thermal convection in rotating stratified spherical layers, *Science* **290**, 1944–1947, 2000.